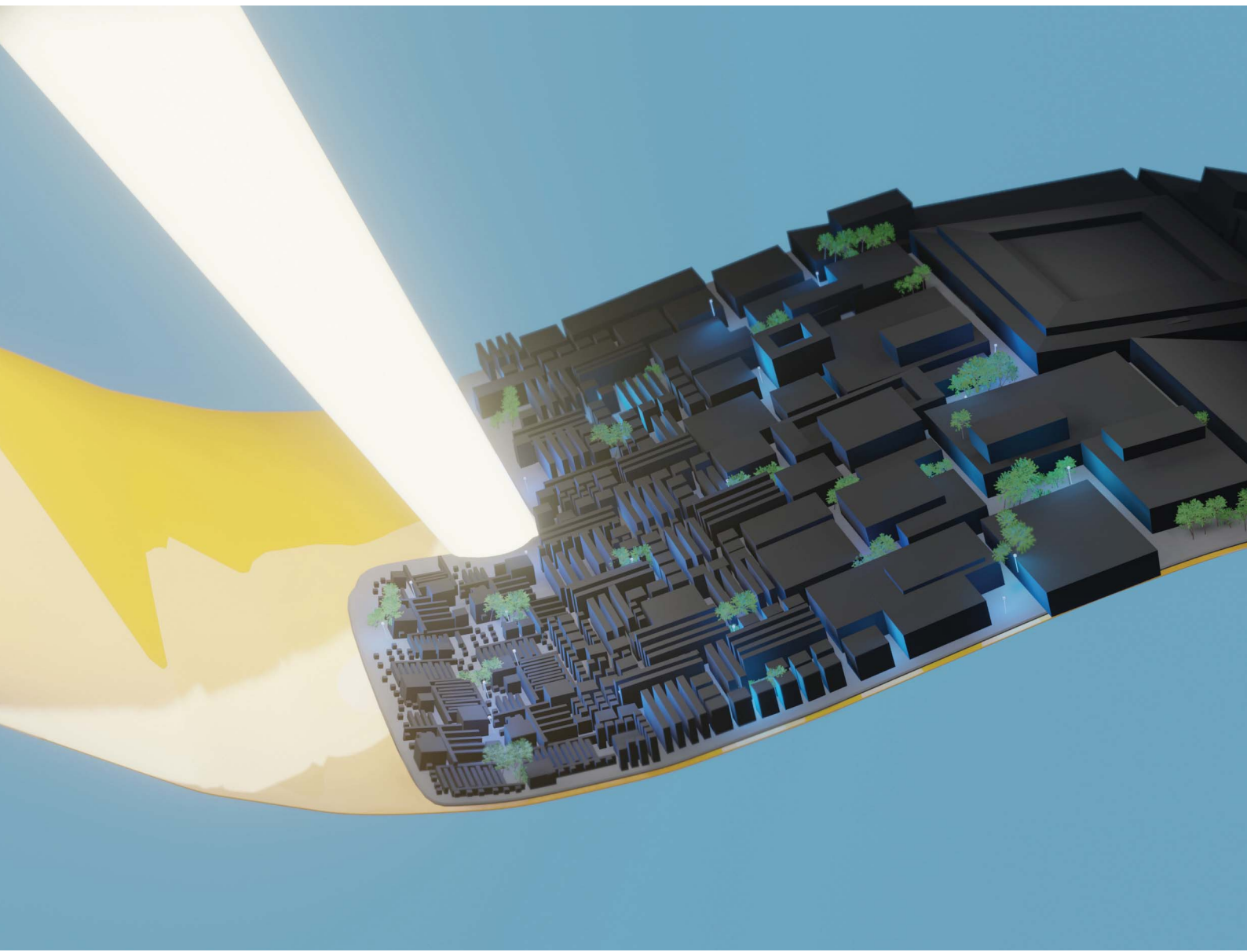


# Sustainable Energy & Fuels

Interdisciplinary research for the development of sustainable energy technologies  
[rsc.li/sustainable-energy](http://rsc.li/sustainable-energy)



ISSN 2398-4902



Cite this: *Sustainable Energy Fuels*, 2021, **5**, 1235

## Recent trends in graphene supercapacitors: from large area to microsupercapacitors

Andres Velasco,<sup>ab</sup> Yu Kyoung Ryu,<sup>a</sup> Alberto Boscá,<sup>ab</sup> Antonio Ladrón-de-Guevara,<sup>c</sup> Elijah Hunt,<sup>a</sup> Jinghan Zuo,<sup>d</sup> Jorge Pedrós,<sup>ab</sup> Fernando Calle<sup>ab</sup> and Javier Martinez  <sup>ae</sup>

Supercapacitors are being increasingly used as energy storage systems. Graphene, with its huge specific surface area, superior mechanical flexibility and outstanding electrical properties, constitutes an ideal candidate for the next generation of wearable and portable devices with enhanced performance. Since Stoller described the first graphene supercapacitor in 2008, significant developments have been made during this last decade in the development of new graphene-based electrodes. In this way, the specific capacitance has been improved from 135 to 2585 F g<sup>-1</sup> and the cyclability has been enhanced from a capacitance retention of just over 80% after 1000 cycles to almost 100% after 20 000 cycles. This review describes how 3-dimensional porous graphene electrodes have been improved recently, from using large area processing techniques to microsupercapacitors. Specifically, (a) the use of graphene foam to obtain large area electrodes, (b) the development of the direct laser writing technique for fast, one-step, and low-cost production of graphene-based supercapacitors, (c) their miniaturization in the form of integrated microsupercapacitors and (d) their functionalization with different pseudocapacitive and electric double-layer capacitor materials to obtain higher capacitance values will be the topics discussed in this perspective.

Received 16th December 2020  
Accepted 29th January 2021

DOI: 10.1039/d0se01849j  
[rsc.li/sustainable-energy](http://rsc.li/sustainable-energy)

## 1 Introduction

Supercapacitors are energy storage devices, which, in contrast to batteries, show a high power performance, with short charge and discharge times and almost no degradation over long-term cycling.<sup>1–4</sup> However, these devices cannot match the high energy density achievable by batteries.<sup>5</sup> In order to get both high power and high energy density at the same time, the coupling of supercapacitors and batteries as hybrid energy storage systems has been actively explored during the last few years for new applications such as electric vehicles.<sup>6–8</sup> The development of the next generation of supercapacitors that will be components in wearable electronics for self-charging devices, especially in the field of the Internet of Things (IoT), is also one of the fundamental challenges that are currently taken care of.<sup>9–13</sup>

Supercapacitors can be divided in two types according to the charge storage mechanism: electric double-layer capacitors (EDLCs) and pseudocapacitors, plus their hybrid combinations. EDLCs store energy electrostatically as image charges to the ions of the electrolyte, by an electric double layer surrounding the electrode–electrolyte interface, as modeled by Gouy–Chapman–Stern.<sup>14</sup> This physical process, through non-faradaic charge transfer, is reversible at very high rates and can reach very high powers, while the energy density is small, limited by the 0.18 electrons that every carbon atom can store.<sup>15</sup> Fig. 1a shows a simplified scheme of an EDLC. Pseudocapacitors, on the other hand, make use of fast and reversible surface redox reactions of active materials in electrodes, such as conductive polymers or metal oxides, to increase the amount of charge that can be stored, at the expense of reducing the power and cyclability of the device<sup>16,17</sup> (scheme represented in Fig. 1b). The main components of a supercapacitor are the electrodes, the corresponding current collectors, a separator between them and an electrolyte, as represented in the scheme shown in Fig. 1c. The electrolyte can be a liquid solvent or a solid-state or quasi-solid-state material<sup>18,19</sup>. When the electrochemical performance of a material as a potential electrode is of interest, rather than the performance of the whole supercapacitor, the measurements are taken in a three-electrode configuration, as depicted in Fig. 1d. Here, the components are a reference electrode, which is used to be able to locate electrochemical features at the

<sup>a</sup>Instituto de Sistemas Optoelectrónicos y Microtecnología, Universidad Politécnica de Madrid, Av. Complutense 30, Madrid 28040, Spain. E-mail: [javier.martinez@upm.es](mailto:javier.martinez@upm.es)

<sup>b</sup>Departamento de Ingeniería Electrónica, E.T.S.I de Telecomunicación, Universidad Politécnica de Madrid, Av. Complutense 30, Madrid 28040, Spain

<sup>c</sup>Hajim School of Engineering and Applied Physics, University of Rochester, Rochester, NY 14627, USA

<sup>d</sup>School of Materials Science and Engineering, Beihang University, Beijing 100191, China

<sup>e</sup>Departamento de Ciencia de Materiales, E.T.S.I de Caminos, Canales y Puertos, Universidad Politécnica de Madrid, C/ Profesor Aranguren s/n, Madrid 28040, Spain



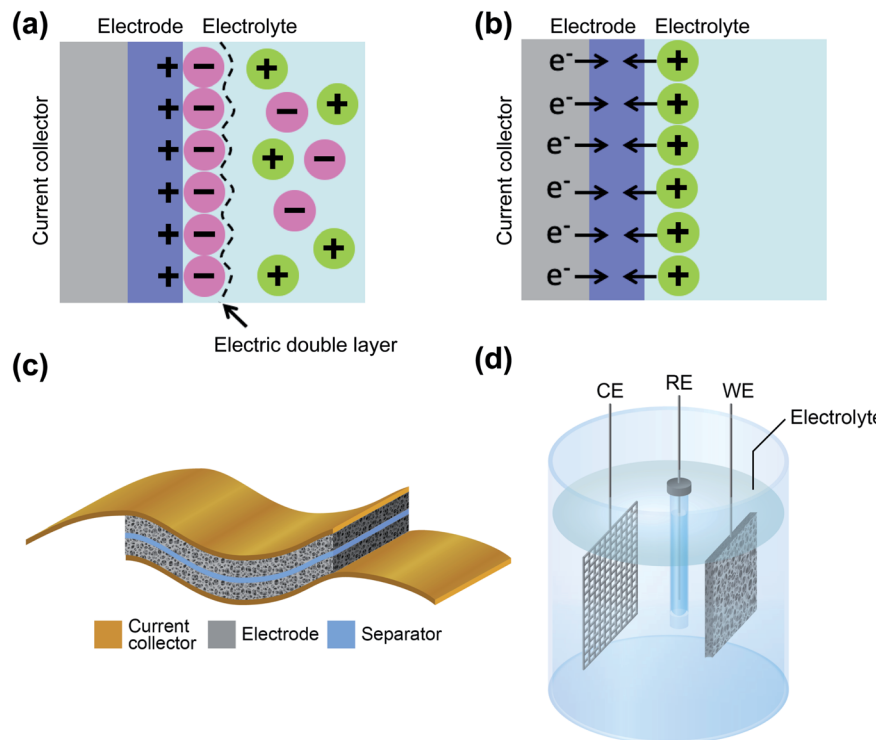


Fig. 1 Scheme of (a) an electric double-layer capacitor and (b) a pseudocapacitor. (c) Schematic drawing of an assembled supercapacitor with a sandwich structure showing current collectors, electrodes and the separator, as used in two-electrode measurements. (d) Schematic drawing of a three-electrode measurement set-up showing a reference electrode, a Pt mesh as the counter electrode and one supercapacitor electrode as the working electrode.

right potentials, a counter electrode, and the electrode under study as the working electrode, all immersed into the electrolyte. However, to determine the charge transfer performance of the full device, a two-electrode measurement is needed, using only a working and a counter electrode that correspond, respectively, to the cathode and anode of the supercapacitor<sup>20</sup>. In order to compare the performance of supercapacitors built with different carbon materials and pseudocapacitive elements, their designs and standard figures-of-merit should match.<sup>21</sup> The main relevant factor regarding supercapacitors is the capacitance, which is the amount of charge that the device can store in relation to the total change in its electric potential. However, the capacitance, in farads, is a meaningless number if it is not normalized by the total mass of the electrodes, or by the volume or area the device occupies. For regular supercapacitors, gravimetric or specific values are considered the most important figures-of-merit, normalized by the mass of the active material, in  $\text{F g}^{-1}$ . Other relevant factors, also reported in this normalized format, are the specific energy density, in  $\text{W h kg}^{-1}$ , and the specific power density, in  $\text{W kg}^{-1}$ , of the device. For the specific case of thin film electrodes and microsupercapacitors, gravimetric values are not as relevant as the mass of the electrodes is typically negligible; therefore these metrics are typically given as areal or volumetric values.<sup>22,23</sup>

Among the several electrode candidates for optimal supercapacitors, graphene has attracted increasing attention due to its striking mechanical, optical and electrical properties and

several effective strategies to synthesize it have been developed and optimized, since its discovery in 2004.<sup>24</sup> Specifically in the energy storage field, its high potential as a next generation supercapacitor electrode is due to three main reasons:

(a) Graphene has the highest known surface area of  $2630 \text{ m}^2 \text{ g}^{-1}$  (ref. 25) and a very low theoretical density of  $2.28 \text{ g cm}^{-3}$ .<sup>26</sup> With these characteristics, the material has simultaneously a high packing density capability and a very large specific surface area for the interaction of electrons and ions.

(b) It presents an excellent electrical conductivity, with very high mobilities that can reach  $200\,000 \text{ cm}^2 \text{ V}^{-1} \text{ s}^{-1}$  at room temperature,<sup>27-29</sup> which enables the fast transfer of electrons and ions through the different device interfaces (electrode/electrolyte and electrode/collector). Also because of the high electrical conductivity, graphene can act simultaneously as an active material and current collector, avoiding the use of extra materials such as binders and additives.

(c) Graphene also shows high mechanical strength, with a Young's modulus of 1 TPa and a demonstrated reversible strain up to 25%,<sup>30</sup> which makes it suitable for its application in flexible and printable electronics, maintaining a high capacitance retention.

Graphene in four dimensional structures (0D to 3D) has been explored as a component for supercapacitors, since the size and morphology of a material have influence on its physical and chemical properties.<sup>31</sup> Among them, 3D graphene-based structures are the most studied because they have an intrinsic



interconnected pore structure that provides a large surface area for interaction with ions and electrons and allows a high mass loading of pseudocapacitive materials, characteristics that are fundamental for highly performing supercapacitors. Consequently, three-dimensional graphene structures<sup>32–34</sup> constitute the focus of the present review, with a special emphasis on the most promising techniques for making 3D graphene electrodes in terms of the achievable surface area, capacity, cyclability, cost-effectiveness and their integration in novel functional applications: (a) graphene foam (GF), (b) graphene materials fabricated by the direct laser writing method (DLW) and (c) graphene as an electrode in microsupercapacitors (MSCs).

(a) Within the family of 3D sponge graphene structures,<sup>35</sup> graphene foam (GF) obtained from the reduction of graphene oxide (rGO) by chemical methods<sup>36–39</sup> and by chemical vapor deposition (CVD)<sup>40–43</sup> represents the focus in Section 2.1. The improvement of its energy density and operating voltage window as a supercapacitor by filling it with other carbon-based materials such as carbon nanotubes (CNTs)<sup>44–46</sup> or pseudocapacitive materials such as metal oxides,<sup>47–49</sup> metal hydroxides<sup>50–53</sup> and conductive polymers<sup>54–57</sup> is also discussed within the section.

(b) The direct laser writing method (DLW) applied to produce materials such as laser reduced graphene oxide (LrGO) or laser induced graphene (LIG) was developed by El-Kady *et al.*<sup>58,59</sup> and constitutes the focus of Section 2.2. The optimization of the fabrication process will lead to the one-step, low-cost and fast production of porous graphene-based supercapacitors. Moreover, the DLW technique bridges the gap between large area electrodes and microelectrodes,<sup>60</sup> making it a very versatile technology worth developing further. As in the case of graphene foam, the performance improvement of supercapacitors based on LrGO or LIG by the addition of pseudocapacitive or EDLC materials<sup>61,62</sup> is discussed within the section.

(c) Finally, in Section 2.3, microsupercapacitors (MSCs) based on 3D graphene are discussed, since they are fundamental for enabling new applications that are useful in many industries, from complementing batteries for better power management to their integration with energy harvesters in self-powering modules. MSCs can be fabricated on flexible substrates and show better power performance and cyclability than batteries, extending the lifetime of the system and making them virtually maintenance-free, being the last requirement fundamental for medical applications. Wireless sensors for the Internet of Things, wearable electronics and implantable medical devices are examples of fields where microsupercapacitors play a key role.<sup>22,63</sup>

In Section 3, the regions in the Ragone plot show the evolution and future tendencies of the graphene electrodes described in Section 2.

## 2 Graphene electrodes

### 2.1 Electrodes fabricated with graphene foam

As mentioned in the Introduction, due to its large surface area and high conductivity, graphene was used for the first time as

an electrode for supercapacitors by Ruoff's group.<sup>25</sup> Since then, to reduce the agglomeration of graphene sheets to maximize the accessible surface area and the creation of large area supercapacitors constitute strategies that are continuously sought. One of the successful approaches up to now has been the use of graphene foam (GF) synthesized by CVD.<sup>64</sup> By means of CVD processing, graphene can be grown on copper or nickel foam, and also to a lesser extent on other catalytic metal foam. High quality, single layer graphene can be grown on copper foam, but this thin structure collapses easily when removing the metal support. By using nickel foam, multilayer graphene is grown and by removing carefully the metal template, a self-standing 3D graphene foam structure is formed. This graphene foam allows building flexible, lightweight electrodes with an area of several  $\text{cm}^2$  and heights in the order of millimeters with a high conductivity. The interconnected network of macroscopic, open pores allows a rapid diffusion of the electrolyte ions. Nickel foam can also be used as a template to form rGO foam from chemical synthesis.<sup>65,66</sup> The disadvantage of this type of graphene foam is that the typical diameter of its pores, in the range of 100 to 500 microns, is quite large. This size of the pores is determined by the diameter of the pores of the initial metal foam. A solution is using graphene foam as a conductive scaffold for the deposition or filling of pseudocapacitive and/or other carbon elements to create highly efficient composites. The graphene foam provides outstanding conductivity and structural stability. The added material of the composite, in intimate contact with graphene, creates faster and shorter transfer paths of electrons and ions for achieving a higher power density. The common composite partners of graphene foam have been metal oxides,<sup>67–71</sup> conductive polymers<sup>57,72–76</sup> or metal hydroxides<sup>53,77,78</sup> mainly because both types of materials are low-cost and already well known in the field of pseudocapacitors. Among the metal oxides, several bimetallic oxides have demonstrated higher electrical conductivity and redox activity than monometallic oxides such as  $\text{ZnO}$ ,  $\text{NiO}$  or  $\text{Co}_3\text{O}_4$ . Therefore, bimetallic oxides have been used for filling the graphene foam.<sup>79–83</sup> Yu *et al.*<sup>79</sup> deposited  $\text{NiCo}_2\text{O}_4$  nanoneedles on graphene foam, achieving a specific capacity of  $1588 \text{ F g}^{-1}$  at  $1 \text{ A g}^{-1}$ . Sun *et al.*<sup>80</sup> used  $\text{NiCo}_2\text{O}_4$  nanoparticles as pseudocapacitive materials and achieved a specific capacity of  $2300 \text{ F g}^{-1}$  at  $1 \text{ A g}^{-1}$ , with a capacitance retention of up to 92% after 4000 cycles at  $10 \text{ A g}^{-1}$ . Conductive polymers provide greater electrical conductivity and structural stability than some metal oxides. Pedrós *et al.*<sup>57</sup> electrodeposited a sponge of polyaniline (PANI) nanofibers, 100 nm thick and several microns long, that filled partially the GF pores. They demonstrated that with only an 11% coverage of the pores, it is possible to obtain high gravimetric and volumetric capacitances of  $1474 \text{ F g}^{-1}$  and  $86 \text{ F cm}^{-3}$  at  $0.47 \text{ A g}^{-1}$ , respectively. In this case the capacitance retention was up to 83% after 15 000 cycles. In some studies, ternary composites have been explored as well,<sup>84,85</sup> where graphene foam is paired with two different pseudocapacitive elements or a pseudocapacitive element plus an electric double-layer one. For example, Tseng *et al.*<sup>85</sup> added activated carbon (electric double-layer material) and  $\text{MnO}_2$  (pseudocapacitive material) to graphene foam to form a composite.



One of the strategies for increasing the power density and the operating potential window of graphene foam-based electrodes, while maintaining the highest energy density possible, consists in the fabrication of asymmetric supercapacitors.<sup>77,86-90</sup> In the work of Zhang *et al.*,<sup>86</sup> an asymmetric supercapacitor composed of graphene foam/MnO<sub>2</sub> and graphene foam/polypyrrole electrodes demonstrated a stable operating voltage window of 1.8 V and a capacitance retention of around 90% after 10 000 cycles. In another remarkable study, Saeed *et al.*<sup>90</sup> fabricated an asymmetric supercapacitor consisting of a novel graphene foam/CNTs/MoO<sub>3</sub> ternary composite as the positive electrode and a graphene foam/CNT composite as the negative electrode. The scheme of the fabrication process is shown in Fig. 2a. This asymmetric cell demonstrated an outstanding capacitance retention of 94% after 10 000 cycles and an operating voltage window of 1.6 V. The graphene foam/CNTs/MoO<sub>3</sub> electrode exhibited a high specific capacitance of 1503 F g<sup>-1</sup> at 1 A g<sup>-1</sup>, see Fig. 2b, as well as an exceptional capacitance retention of 96.5% after 10 000 cycles.

In this section, we have observed that the fabrication of graphene foam/pseudocapacitive material-based composites is the strategy of choice to optimize the performance of graphene as an electrode for supercapacitors, but generally at the expense of a cycling stability reduction. Therefore, new materials such as transition metal sulfides are investigated as potential pseudocapacitive elements.<sup>91-100</sup> As represented in the scheme shown in Fig. 2c, Kamali-Heidari *et al.*<sup>96</sup> grew hierarchically Ni<sub>3</sub>S<sub>2</sub> nanorods on CVD graphene foam, to achieve a specific

capacitance of 1900 F g<sup>-1</sup> at a current density of 1 A g<sup>-1</sup> (Fig. 2d) and a capacitance retention of 96% after 2000 cycles. Kang *et al.*<sup>97</sup> grew NiCo<sub>2</sub>S<sub>4</sub> nanowires on CVD graphene foam, which provided a specific capacitance of 1454 F g<sup>-1</sup> at 1.3 A g<sup>-1</sup> and a capacitance retention of 96% after 3000 cycles at 13 A g<sup>-1</sup>. These recent results show that under optimization, new material combinations could provide higher electrical conductivity and structural stability than metal oxides and conductive polymers.

Another direction to improve the capacitance of graphene foam based supercapacitors is the maximization of the electrochemically available surface area and the minimization of the collapse or restacking of the graphene foam pores. This can be achieved by optimizing the metallic foam used as the template. As we explained at the beginning of this section, the diameter of the pores from typical commercial Cu or Ni foam lies in the range of 100 to 500 microns. The density and the diameter of Cu or Ni foam can be tuned by adjusting the catalyst particle size and the growth temperature. In this way, Drieschner *et al.*<sup>101</sup> fabricated Cu and Ni foam with smaller pores that were produced by CVD, and graphene foam with pore sizes in the range of 0.5 to 30 microns, which presented an electrochemically available surface area 10 000 times larger than that of the graphene foam fabricated by using commercial metal templates. These small pore GFs also presented a higher mechanical stability after the removal of the template by etching and a capacitance retention of almost 100% after 10 000 cycles at 4 mA cm<sup>-3</sup>. Another group achieved GF with 1 μm size

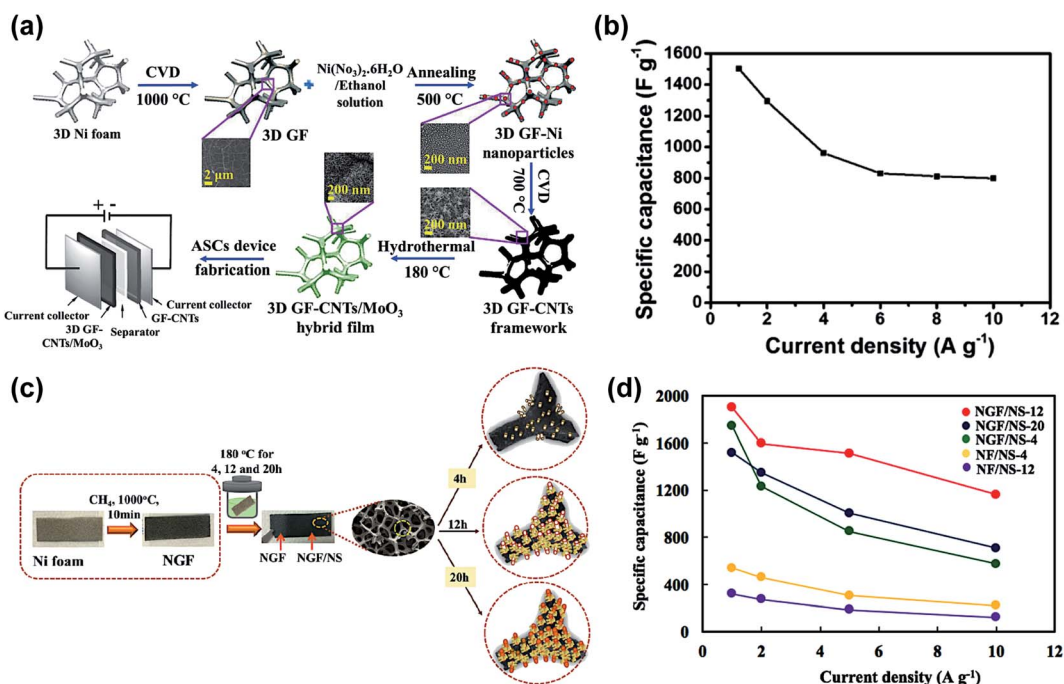


Fig. 2 Different examples of graphene foam (GF) supercapacitors: (a) schematic diagram illustrating all steps involved in the synthesis of 3D GF/CNTs/MoO<sub>3</sub> hybrid film-based electrode and the asymmetric supercapacitor device and (b) specific capacitance vs. current density obtained with this supercapacitor. (a) and (b) are reproduced with permission from ref. 90. Copyright 2018 Elsevier B.V. (c) Schematic diagram of the fabrication process of the Ni-GF/Ni<sub>3</sub>S<sub>2</sub> nanocomposite electrode and (d) specific capacitances of different electrode materials plotted as a function of current density. (c) and (d) are reproduced with permission from ref. 96. Copyright 2018 Elsevier B.V.

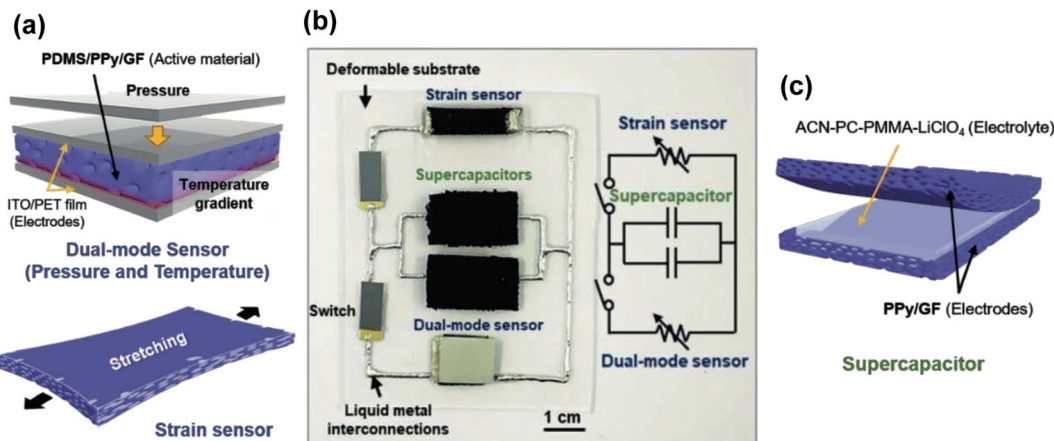


Fig. 3 (a) Schematic drawing of a pressure/temperature sensor and a strain sensor based on polypyrrole/graphene-foam material. (b) Picture showing the electric circuit connecting these elements with two supercapacitors using liquid metal interconnects. (c) Schematic drawing of the PPy/GF sandwich supercapacitor. Reproduced with permission of ref. 106. Copyright 2018 Wiley-VCH Verlag GmbH & Co. KGaA, Weinheim.

pores by CVD using sintered Ni nanoparticles as template.<sup>102</sup> Recently, a graphene foam composed mainly of mono- and bi-layers was achieved by designing a Ni–Cu foam alloy.<sup>103</sup> Another group, starting from commercial Ni foam, created a Ni–Cu foam alloy where they further synthesized Cu–Ni micro-branches of 2–5 microns in diameter and 20–30 microns in length. These highly dense microbranches reduced the percentage of empty porous space in the commercial Ni foam by

up to 63%.<sup>104</sup> 3D-printed porous silica templates designed with different pore/void sizes and complex architectures were used to obtain GF by CVD with a large surface area, 994.2 m<sup>2</sup> g<sup>-1</sup>, and good mechanical properties.<sup>105</sup>

Finally, graphene foam and its composites have been proven to have high potential in advanced applications. For example, GF synthesized by CVD and coated with polypyrrole (PPy) has shown outstanding flexibility (180°) and stretchability (up to

Table 1 Graphene foam-based electrodes

Graphene foam fabrication method	Active material	Specific capacitance (F g <sup>-1</sup> )	Retention (%) after a number of cycles	Year	Ref.
CVD	Ni(OH) <sub>2</sub> nanoflakes	900 at 1 A g <sup>-1</sup>	98% at 2 A g <sup>-1</sup> after 3000	2015	53
rGO	NiCo <sub>2</sub> S <sub>4</sub> nanoparticles	1526 at 1 A g <sup>-1</sup>	83% at 10 A g <sup>-1</sup> after 2000	2015	98
CVD	NiCo <sub>2</sub> O <sub>4</sub> flowers	1402 at 1 A g <sup>-1</sup>	76.6% at 5 A g <sup>-1</sup> after 5000	2015	81
CVD	NiCo <sub>2</sub> O <sub>4</sub> nanoneedles	1588 at 1 A g <sup>-1</sup>	85.7% at 10 A g <sup>-1</sup> after 2000	2015	79
CVD	PANI nanofibers	1474 at 0.47 A g <sup>-1</sup>	83% at 28 mA cm <sup>-2</sup> after 15 000	2016	57
rGO	Ni–Co layered double hydroxide nanowires	1041 at 2.5 mA cm <sup>-2</sup>	95% at 12.5 mA cm <sup>-2</sup> after 2000	2016	77
rGO	NiCo <sub>2</sub> O <sub>4</sub> nanoparticles	2300 at 1 A g <sup>-1</sup>	92% at 10 A g <sup>-1</sup> after 4000	2016	80
CVD	Co(OH) <sub>2</sub> nanoflakes	1636 at 0.5 A g <sup>-1</sup>	75% at 20 mV s <sup>-1</sup> after 1000	2017	78
CVD	V <sub>2</sub> O <sub>5</sub> flowers	1235 at 2 A g <sup>-1</sup>	92% at 4 A g <sup>-1</sup> after 5000	2017	70
CVD	Mn <sub>3.63</sub> Co <sub>5.37</sub> S <sub>8</sub> nanohoneycombs	1938 at 5 A g <sup>-1</sup>	82% at 50 A g <sup>-1</sup> after 4000	2017	92
RGO	H–CoMoO <sub>4</sub> nanoplates	1472 at 1 mA cm <sup>-2</sup>	92.3% at 15 mA cm <sup>-2</sup> after 3000	2017	88
CVD	NiO nanoflakes	1782 at 1 A g <sup>-1</sup>	90.2% at 1 A g <sup>-1</sup> after 5000	2017	71
CVD	ZnCo <sub>2</sub> O <sub>4</sub> nanowires	1626 at 1 A g <sup>-1</sup>	76.4% at 1 A g <sup>-1</sup> after 5000	2017	82
CVD	NiCo <sub>2</sub> S <sub>4</sub> /Co <sub>x</sub> Ni <sub>(3-x)</sub> S <sub>2</sub> core/shell nanowires	1950 at 1.25 A g <sup>-1</sup>	93% at 50 mA cm <sup>-2</sup> after 5000	2017	91
RGO	Co <sub>3</sub> S <sub>4</sub> nanoflakes	2314 at 2 mV s <sup>-1</sup>	92.6% at 100 mV s <sup>-1</sup> after 1000	2017	94
CVD	NiCo <sub>2</sub> O <sub>4</sub> @MnO <sub>2</sub> core–shell nanowires	2125 at 1 A g <sup>-1</sup>	93.4% at 20 A g <sup>-1</sup> after 5000	2017	84
CVD	Activated carbon and MnO <sub>2</sub> flowers	813 at 1 A g <sup>-1</sup>	98.4% at 20 mV s <sup>-1</sup> after 1000	2018	85
CVD	NiO nanoflakes	1062 at 1 A g <sup>-1</sup>	90.6% at 1 A g <sup>-1</sup> after 5000	2018	68
CVD	CNT and MoO <sub>3</sub> nanoplates	1503 at 1 A g <sup>-1</sup>	96.5% at 8 A g <sup>-1</sup> after 10 000	2018	90
CVD	Ni <sub>3</sub> S <sub>2</sub> nanorods	1900 at 1 A g <sup>-1</sup>	96% at 5 A g <sup>-1</sup> after 2000	2018	96
CVD	NiCo <sub>2</sub> S <sub>4</sub> nanowires	1454.6 at 1.3 A g <sup>-1</sup>	96% at 13 A g <sup>-1</sup> after 3000	2018	97
RGO	NiCo <sub>2</sub> S <sub>4</sub> nanosheets	2526 at 2 A g <sup>-1</sup>	77% at 20 A g <sup>-1</sup> after 2000	2018	93
RGO	NiGa <sub>2</sub> S <sub>4</sub> nanoparticles	2124.34 at 1 A g <sup>-1</sup>	94.2% at 9 A g <sup>-1</sup> after 5000	2019	99
CVD	Ni <sub>3</sub> S <sub>2</sub> nanoparticles	2585 at 1 A g <sup>-1</sup>	89% at 20 A g <sup>-1</sup> after 5000	2020	100
CVD	N-doping NiMoO <sub>4</sub> nanoflakes	1913 at 1 A g <sup>-1</sup>	90.7% at 100 mV s <sup>-1</sup> after 3000	2020	83

50% strain).<sup>74</sup> These properties were used to fabricate a device with a pressure-temperature dual sensor connected to a supercapacitor, where the common active material of both components was a PDMS/PPy/GF/composite.<sup>106</sup> These devices could be bent up to 5% and exhibit almost no performance degradation over 10 000 cycling under load pressure, which shows their suitability for stretchable and wearable electronics. This integrated device is shown in Fig. 3.

To conclude this section, we provide Table 1, where we have summarized the graphene foam based electrodes (with their corresponding references) that we have found to present the best performance in terms of specific capacitance and cyclability during the last 5 years. We have arranged them in chronological order, to track the trends in performance and chosen composite materials over time.

## 2.2 Electrode fabricated by laser direct writing

Graphene foam described in the previous section produces supercapacitors with high specific energy, capacitance retention and a large area. GF also presents a high surface area, which can be further optimized by designing the size of the pores. However, the total processing time of CVD is long and the cost is still relatively high compared to other techniques. Regarding the obtention of rGO foam by chemical reduction of GO, it is more cost-effective and also suitable for large area production compared to CVD, but this method has not yet optimized the reduction efficiency, which hinders the conductivity of the material. Hence, an alternative technique is direct laser writing (DLW) processing, which constitutes a low-cost, fast, single step, large area reduction technique to produce 3D porous graphene. DLW can be applied to reduce GO under laser irradiation (LrGO).<sup>58</sup> First, a thin layer of graphene oxide is deposited onto a substrate. Then, the surface of the GO is irradiated with a commercial laser. The incident light exfoliates and reduces the stacked GO sheets simultaneously, creating a porous, conductive material, only in the areas exposed to the laser. The process increases the surface area available for the electrolyte ions and leaves a very low percentage of oxygen content. A scheme of the process is summarized in Fig. 4a. Another approach to obtain 3D porous graphene is the production of laser-induced graphene (LIG) from a polymer substrate by pyrolysis,<sup>107–113</sup> as presented in Fig. 4b. Finally, the graphene oxide (in the LrGO case) or initial polymer substrate (in the LIG case) can be functionalized/mixed with another active material before the laser irradiation in order to control the morphology of the produced graphene, dope it or produce a composite in a single step, as summarized in Fig. 4c.

The main mechanisms to reduce graphene oxide by DLW are through the photochemical effect (laser wavelengths ( $\lambda$ ) below 400 nm), the photothermal effect (laser wavelengths ( $\lambda$ ) above 400 nm) and under certain wavelengths and irradiation conditions, through both effects.<sup>114,115</sup> In the case of the photochemical effect, for lasers with the wavelength in the ultraviolet (UV) or near UV region, the energy of the incident photons breaks the chemical bonds of the oxygen-containing radicals that are attached to the graphene surface such as  $-\text{COOH}$  or

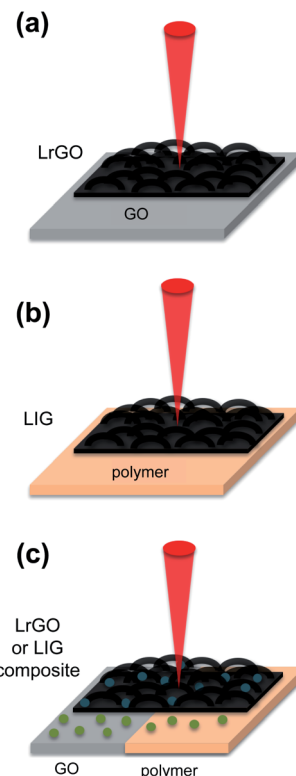


Fig. 4 Schemes of direct laser writing (DLW) applied on (a) graphene oxide to reduce it (LrGO), (b) a polymer substrate to produce graphene (LIG), and (c) graphene oxide or a polymer substrate functionalized with a material deposited onto them (represented by the green spheres) before the laser irradiation, in order to influence the final morphology of the produced graphene or fabricate a graphene/pseudocapacitive composite in a single step. In most of the cases, the functionalizing material is chemically modified during the DLW process, as indicated by the change of the color of the spheres after laser irradiation.

$-\text{OH}$ , producing LrGO. In the case of the photothermal effect, for lasers with higher wavelengths, especially in the infrared (IR) or near infrared (NIR) region, the high energy density of the incident light is absorbed by the graphene oxide and as a consequence, a very high thermal heat is concentrated locally. This generated heat breaks the chemical bonds of the oxygen-containing radicals, producing LrGO. To produce LIG from an initial polymeric substrate, a high temperature is needed to rearrange the chains into the graphene structure; therefore, lasers with wavelengths that induce the photothermal effect are required.<sup>62,116</sup> The most commonly used polymeric substrate is commercial polyimide. However, LIG has been fabricated from a wide variety of substrates, such as wood,<sup>117</sup> phenolic resin,<sup>118</sup> lignin,<sup>119</sup> polyether ether ketone (PEEK)<sup>110</sup> or carbon nanospheres.<sup>120</sup>

The laser irradiation parameters such as the incident wavelength, power intensity, scanning speed and step size have a strong influence on the quality of the produced 3D porous graphene and its performance as a supercapacitor. Therefore, the parameters of each laser setup must be calibrated first to obtain optimized LrGO or LIG. For example, Bhattacharjya



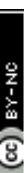


Table 2 LiG and LrGO-based electrodes

Starting material	Added active material to LiG/LrGO	Final material	Laser (wavelength & writing parameters)	Capacitance	Energy density	Power density	Retention (%) after a number of cycles	Year	Ref.
Polyimide	—	LiG	522 nm, 140 mW, 500 fs pulse, 1 MHz, 2 J cm <sup>-2</sup> , 1 mm s <sup>-1</sup> speed	800 $\mu$ F cm <sup>-2</sup> at 10 mV s <sup>-1</sup>	—	—	96% after 3000 at 0.3 mA cm <sup>-2</sup>	2015	112
GO	—	LiGO	Nd:YVO <sub>4</sub> , 355 nm, 244 mW, 20 ns pulse, 0.9 kHz, 2.5 mm s <sup>-1</sup> speed, 2.5 $\times$ 10 <sup>-4</sup> J mm <sup>-2</sup>	106 $\mu$ F cm <sup>-2</sup> at 0.3 V s <sup>-1</sup>	—	—	92.5% after 5000 at 0.6 V s <sup>-1</sup>	2016	125
GO	MnO <sub>2</sub>	LiGO + MnO <sub>2</sub>	CO <sub>2</sub> , 10.6 $\mu$ m, 2 W, 1 pass, 394 $\mu$ cm <sup>-1</sup> pulse density	1.72 F g <sup>-1</sup> at 1 mA cm <sup>-2</sup>	0.409 mW h cm <sup>-3</sup>	537 W cm <sup>-3</sup>	95% after 2000 at 1 mA cm <sup>-2</sup>	2016	136
GO	—	LiGO	355 nm, ns frequency, 5 m s <sup>-1</sup> speed	3.9 mF cm <sup>-2</sup> at 0.3 mA cm <sup>-2</sup>	0.98 mW h cm <sup>-3</sup>	300 mW cm <sup>-3</sup>	93% after 20 000 at 1 V s <sup>-1</sup>	2016	128
GO	PEDOT	LiGO + PEDOT	IR laser 788 nm, 100 mW	43.75 mF cm <sup>-2</sup> at 0.2 mA cm <sup>-2</sup>	—	—	83.6% after 1000 at 0.2 mA cm <sup>-2</sup>	2017	130
V <sub>2</sub> O <sub>5</sub> nanobelts and GO mixture	—	LiGO + VO <sub>x</sub>	1064 nm, 3 W, 10 $\mu$ s pulse, 20 kHz, 2 m s <sup>-1</sup> speed	252 F g <sup>-1</sup> at 1 A g <sup>-1</sup>	—	—	92% after 10 000 at 100 A g <sup>-1</sup>	2017	140
Polyimide	N-doping PEDOT	N-LiG + PEDOT	CO <sub>2</sub> , 10.6 $\mu$ m, 5 W, 1 pass, 14 $\mu$ s pulse	790 $\mu$ F cm <sup>-2</sup> at 50 $\mu$ A cm <sup>-2</sup>	—	—	96% after 10 000 at 0.2 mA cm <sup>-2</sup>	2018	137
Phenolic resin	—	LiG	405 nm, 500 mW, 200 mm s <sup>-1</sup> speed	0.78 mF cm <sup>-2</sup> at 500 mV s <sup>-1</sup>	—	—	93.78% after 2000 at 1 mA cm <sup>-2</sup>	2018	118
Polyimide	—	LiG	Nd:YAG, 1064 nm, 7.5 A, 11 kHz, 80 mm s <sup>-1</sup> speed	34.7 mF cm <sup>-2</sup> at 0.1 mA cm <sup>-2</sup>	1 mW h cm <sup>-3</sup>	11 mW cm <sup>-3</sup>	80% after 3000 at 0.15 mA cm <sup>-2</sup>	2018	107
GO/Co <sub>3</sub> O <sub>4</sub> nanorod mixture	—	LiGO + Co <sub>3</sub> O <sub>4</sub> nanoparticles	KrF excimer, 248 nm, 25 ns, 10 Hz, 400 nJ per pulse per cm	978.1 F g <sup>-1</sup> at 1 A g <sup>-1</sup>	—	—	99.3% after 20 000 at 10 A g <sup>-1</sup>	2018	142
Lignin/PVA mixture	—	LiG	CO <sub>2</sub> , 10.6 $\mu$ m, 1.8–3 W, 2.25 inches s <sup>-1</sup> speed	25.1 mF cm <sup>-2</sup> at 0.05 mA cm <sup>-2</sup>	1 mW h cm <sup>-3</sup>	2 W cm <sup>-3</sup>	99.2% after 12 000 at 2 mA cm <sup>-2</sup>	2018	119
GO	—	LiGO	308 nm, 5 MW, 105 mJ, 100 Hz	299 F g <sup>-1</sup> at 2 mV s <sup>-1</sup>	—	—	97.8% after 4000 at 50 mV s <sup>-1</sup>	2018	127
GO paper	—	LiGO	Nd:YVO <sub>4</sub> pulsed laser, 355 nm, 20 ns pulse, 325 mW, 2 mm s <sup>-1</sup> scan speed	13.8 $\mu$ F cm <sup>-2</sup> at 10 mV s <sup>-1</sup>	—	—	95% after 3400 at 10 mV s <sup>-1</sup>	2019	129
ErGO	—	LiErGO	CO <sub>2</sub> , 10.6 $\mu$ m, 30 W, 0.5 m s <sup>-1</sup> speed, 20 000 Hz, 1 pass	2.32 mF cm <sup>-2</sup> at 10 $\mu$ A cm <sup>-2</sup>	0.46 mW h cm <sup>-2</sup>	0.57 W cm <sup>-2</sup>	100% after 100 000 at 0.166 mA cm <sup>-2</sup>	2019	149
GO	PANI nanofibers	LiGO + PANI	788 nm, 5 mW, 1 pass, 25 min cycle <sup>-1</sup>	442 F g <sup>-1</sup> at 0.18 A g <sup>-1</sup>	—	—	84% after 2000 at 3.7 A g <sup>-1</sup>	2019	139
Polyimide	—	LiG	1064 nm, 7 W, 800 mm s <sup>-1</sup> speed	995 mF cm <sup>-2</sup> at 1 mA cm <sup>-2</sup>	55.9 $\mu$ W h cm <sup>-2</sup>	9.39 mW cm <sup>-2</sup>	98% after 10 000 at 1 mA cm <sup>-2</sup>	2019	131
GO/urea mixture	—	N-LrGO	1064 nm, 0.2 W, 10 ps pulse, 1 MHz, 100 mm s <sup>-1</sup> speed	60.7 mF cm <sup>-2</sup> at 0.5 mA cm <sup>-2</sup>	6.8 $\mu$ W h cm <sup>-2</sup>	0.25 mW cm <sup>-2</sup>	98.7% after 25 000 at 10 mA cm <sup>-2</sup>	2019	132
Carbon nanospheres	—	LiG	CO <sub>2</sub> , 10.6 $\mu$ m, 3.4 W, 1 pass, 3% speed	0.8 mF cm <sup>-2</sup> at 0.078 mA cm <sup>-2</sup>	0.18 mW h cm <sup>-3</sup>	28 W cm <sup>-3</sup>	98.6% after 12 000 at 1.56 mA cm <sup>-2</sup>	2019	120



Table 2 (Contd.)

Starting material	Added active material to LiG/LrGO	Final material	Laser (wavelength & writing parameters)	Capacitance	Energy density	Power density	Retention (%) after a number of cycles	Year	Ref.
Polyimide coated with $\text{Mo}^{6+}$ , $\text{Mn}^{2+}$ and $\text{S}^{2-}$ solution	—	LiG + $\text{MoS}_2$ + $\text{MnS}$	$\text{CO}_2$ , 10.6 $\mu\text{m}$ , 5–10 W, 14 $\mu\text{s}$ pulse, 5–180 $\text{cm s}^{-1}$	58.3 mF ULLK <sub>1</sub> /m <sup>-2</sup> at 50 $\mu\text{A cm}^{-2}$	7 $\mu\text{W h cm}^{-2}$	49.9 $\mu\text{W cm}^{-2}$	93.6% after 10 000 at 1 $\text{mA cm}^{-2}$	2019	145
$\text{GO}/\text{TiO}_2$ nanocrystal solution	—	LiG + O-deficient $\text{TiO}_2$	KrF excimer, 248 nm, 5 Hz, 25 ns pulse, 300 mJ per pulse $\text{cm}^2$	401.7 $\text{F g}^{-1}$ at 1 $\text{Ag}^{-1}$	14.1 $\text{W h tkg}^{-1}$	8.5 $\text{kW kg}^{-1}$	≈100% after 20 000 at 10 $\text{Ag}^{-1}$	2019	141
Polyimide	PEDOT	LiG + PEDOT	$\text{CO}_2$ , 10.6 $\mu\text{m}$ , 4.5 W, 20% speed, 1000 pulses per inch	115.2 $\text{F g}^{-1}$ at 0.5 $\text{Ag}^{-1}$	—	—	97.5% after 4000 at 2.4 $\text{Ag}^{-1}$	2020	138
Kraft lignin	—	LiG	$\text{CO}_2$ , 10.6 $\mu\text{m}$ , 32 W, 20 cm $\text{s}^{-1}$ speed, 1000 pulses per inch	880 $\mu\text{F cm}^{-2}$ at 10 $\text{mV s}^{-2}$	0.152 $\mu\text{W h cm}^{-2}$	25 $\mu\text{W cm}^{-2}$	91% after 10 000 at 0.02 $\text{mA cm}^{-2}$	2020	124
GO	PANI	LiGO + PANI	850 nm, 1200 mW	72 $\text{mF cm}^{-2}$ at 35 $\mu\text{A cm}^{-2}$	2.7 $\text{mW h cm}^{-3}$	81.4 $\text{mW cm}^{-3}$	93.5% after 1000 at 0.7 $\text{mA cm}^{-2}$	2020	133
Polyimide coated with Ni and Co ion ink	—	NiO/ $\text{Co}_3\text{O}_4$ /LiG	$\text{CO}_2$ , 10.6 $\mu\text{m}$ 2.5 W, 100 $\text{mm s}^{-1}$ speed	29.5 $\text{mF cm}^{-2}$ at 0.05 $\text{mA cm}^{-2}$	—	—	99.1% after 10 000 at 0.05 $\text{mA cm}^{-2}$	2020	150

*et al.*<sup>121</sup> found the optimum conditions of their system, a low-cost  $\text{CO}_2$  commercial laser ( $\lambda = 10.6 \mu\text{m}$ ), under an incident power of 30 W, scanning speed of 10  $\text{mm s}^{-1}$  and step size of 100  $\mu\text{m}$  and the worst conditions under an incident power of 30 W, scanning speed of 500  $\text{mm s}^{-1}$  and step size of 500  $\mu\text{m}$ , in order to produce LrGO. This clearly means that under the same incident power, a slower scan speed and a smaller step size mean a higher irradiation time of GO and consequently, a higher removal efficiency of the oxygen-containing radicals from the graphene surface.

Currently, a  $\text{CO}_2$  commercial laser ( $\lambda = 10.6 \mu\text{m}$ ) is the most widely used to produce both LrGO<sup>121,122</sup> and LIG.<sup>123,124</sup> Then, a pulsed laser with the wavelength in the UV region has been used in several studies in order to produce LrGO.<sup>125–129</sup> The principal motivation to use this type of laser is that the level of reduction is very high at short times, since pulses in the order of nanoseconds/femtoseconds can produce incident powers in the order of MW. Different laser systems with intermediate wavelengths between the IR and the UV region have also been employed to produce 3D porous graphene.<sup>130–133</sup> Similar to the DLW approach, as an attempt to maximize the rGO area in minimum time, Xiang *et al.*<sup>134</sup> irradiated GO films electro-sprayed onto stainless steel sheets of 2  $\text{cm}^2$  area for 3 min inside a home-use convection oven (far infrared irradiation) under air conditions. During the irradiation process, within which the chamber of the oven reached 200 °C, the GO film was exfoliated and the oxygen-containing functional groups were decomposed, obtaining rGO porous electrodes with a specific capacitance of 320  $\text{F g}^{-1}$  at 0.2  $\text{Ag}^{-1}$  and a capacitance retention of 94% after 10 000 cycles. Some of the recent examples with all the different lasers are summarized in Table 2, shown at the end of this section.

In the case of electrodes based on 3D porous graphene synthesized by DLW, the pseudocapacitive material fillings have another role in addition to the enhancement of the device performance: their presence minimizes the restacking of the graphene sheets during charge/discharge cycling.<sup>108,135–138</sup> Ladrón-de-Guevara *et al.*<sup>139</sup> coated LrGO ( $\lambda = 788 \text{ nm}$ ) with PANI nanofibers by electrodeposition. The composite electrode presented a specific capacitance of 442  $\text{F g}^{-1}$ , as opposed to the 81  $\text{F g}^{-1}$  value achieved by the bare LrGO electrode, as shown in the graph of Fig. 5a. Fig. 5b to d show the scanning electron microscope (SEM) images of the electrodes in different processing stages. In Fig. 5b, a difference in the morphology before (GO) and after (LrGO) laser irradiation is observed. Fig. 5c shows a close-up image of the exfoliated and reduced GO, marked with a white area in Fig. 5b. Finally, in Fig. 5d, the densification and consequent increase of the surface area in the electrode after the deposition of PANI nanofibers can be observed as compared with the bare LrGO electrode shown in Fig. 5c.

As mentioned above and shown in Fig. 4c, DLW allows the fabrication of a 3D porous graphene/pseudocapacitive material composite in a single step, by irradiating a GO/pseudocapacitive material mixture in the case of LrGO<sup>140–142</sup> or a polymer surface coated with a pseudocapacitive material layer in the case of LIG.<sup>143–145</sup> Yang *et al.*<sup>141</sup> irradiated a  $\text{TiO}_2$  nanocrystals/GO

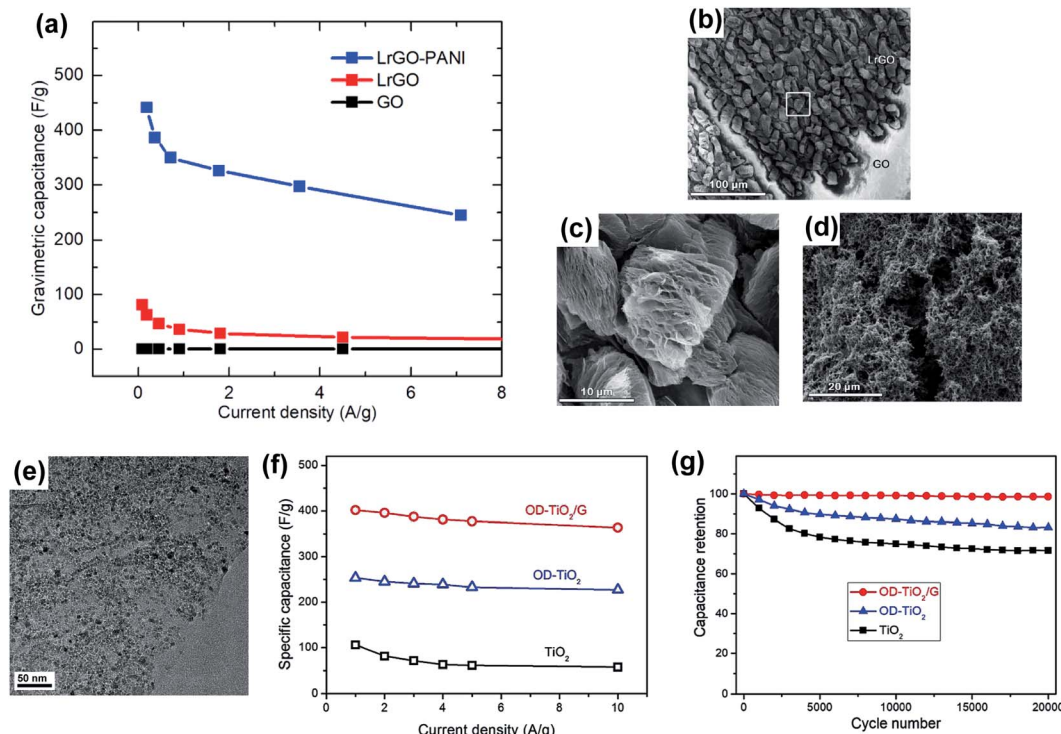


**Fig. 5** (a) Specific capacitance as a function of the current density obtained with a GO electrode (black line), a rGO electrode (red line) and a rGO/PANI nanofiber composite electrode (blue line). This comparison shows the superior performance of the rGO electrode when was coated with the PANI nanofibers. (b) SEM secondary image showing an area before (GO) and after (LrGO) the laser irradiation. (c) SEM secondary image showing an area with LrGO flakes, after laser irradiation. It corresponds to the white area marked in (b). (d) SEM image showing an area with LrGO flakes coated with PANI nanofibers after electrodeposition. (a)–(d) are reproduced with permission from ref. 139. Copyright 2018 Elsevier B.V. (e) A TEM image of an oxygen-deficient TiO<sub>2</sub> nanocrystals/GO composite, which shows a uniform distribution of the nanocrystals over the rGO surface. (f) Specific capacitance as a function of the current density obtained with a TiO<sub>2</sub> electrode (black line), an oxygen-deficient TiO<sub>2</sub> electrode (blue line) and an oxygen-deficient TiO<sub>2</sub>/rGO composite electrode (red line). This comparison was made to show the superior performance of the oxygen-deficient TiO<sub>2</sub>/rGO composite electrode with respect to the other compositions. (g) Cycling stability plot of the composites, where the oxygen-deficient TiO<sub>2</sub>/rGO composite electrode shows almost 100% capacitance retention after 20 000 cycles. (e)–(g) are reproduced with permission from ref. 141. Copyright 2019 Elsevier B.V.

composite with a KrF excimer laser ( $\lambda = 248$  nm, 25 ns pulse), enabling simultaneously the reduction of the GO and the creation of oxygen vacancies on the TiO<sub>2</sub> nanocrystals. A TEM image of the final oxygen-deficient TiO<sub>2</sub> nanocrystals/LrGO composite, presented in Fig. 5e, shows the uniform distribution of the nanocrystals over the LrGO surface. These defects were introduced to increase both the active sites and the electrical conductivity. Measuring this electrode, a specific capacitance of 400 F g<sup>-1</sup> (Fig. 5f) and a barely disturbed capacitance retention after 20 000 cycles (Fig. 5g) were obtained. Clerici *et al.*<sup>143</sup> covered the initial polyimide substrate with a MoS<sub>2</sub> dispersion and then, they irradiated the mixture with a CO<sub>2</sub> laser, producing a MoS<sub>2</sub> sheets/LIG composite. The introduction of an extra material into the initial mixture with GO before laser irradiation can also be done to influence the final structure of LrGO. For example, Lee *et al.*<sup>146</sup> infiltrated Zn by atomic layer deposition on GO before laser irradiation. The presence of Zn influenced the morphology of the obtained LrGO by increasing the total specific surface area. The effect was a four-fold increase in the specific capacitance: from 21 F g<sup>-1</sup> (GO  $\rightarrow$  LrGO) to 83 F g<sup>-1</sup> (GO/Zn  $\rightarrow$  LrGO/Zn).

Finally, 3D porous graphene electrodes fabricated by DLW have been successfully transferred to flexible and stretchable substrates, in view of the rise of wearable and portable electronics. For example, Lamberti *et al.*<sup>113</sup> developed a method to transfer LIG produced from a polyimide substrate onto polydimethylsiloxane (PDMS), as described in the scheme shown in Fig. 6a. They used the LIG/PDMS substrate to fabricate a supercapacitor (Fig. 6b), which presented a capacitance retention of 96% after 10 000 cycles (Fig. 6c) under static conditions and of almost 90% after 1000 cycles under bending conditions (from 0° to 160°). Moreover, several prototypes of 'self-charging power unit' devices, where DLW fabricated LrGO or LIG supercapacitors were coupled to a solar cell, have been recently demonstrated.<sup>147–150</sup> In Fig. 7a, a scheme of one of these self-powered integrated devices is shown: the LIG supercapacitor stores energy from the solar cell and illuminates an LED.<sup>149</sup> Fig. 7b shows a real device. In Fig. 7c, it is shown that the LIG-based supercapacitor presented a capacitance retention of almost 100% after 100 000 cycles at 0.166 mA cm<sup>-2</sup>.

To conclude this section, we provide Table 2, where LrGO and LIG electrodes fabricated with different laser systems and

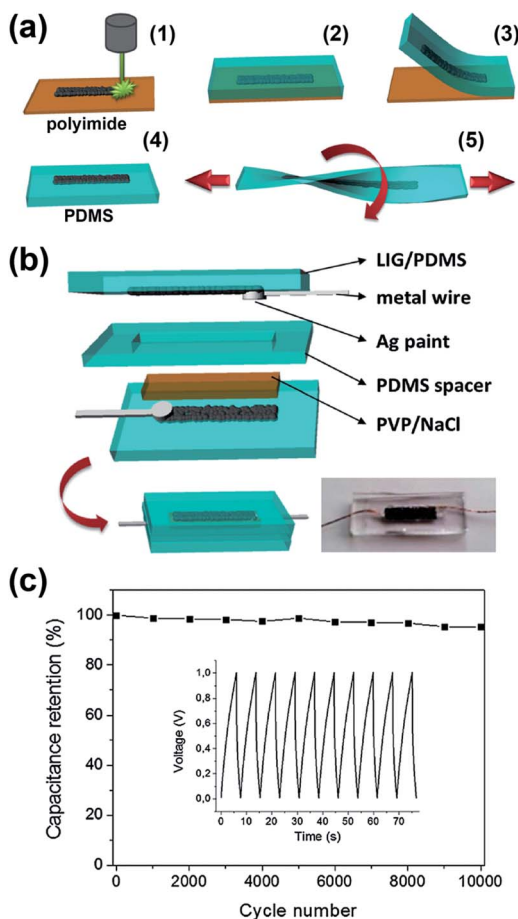


Fig. 6 (a) Scheme of the transfer process of LIG fabricated by DLW on polyimide onto a flexible and stretchable PDMS substrate. (b) Scheme of the structure of a stretchable supercapacitor fabricated using the LIG/PDMS substrates. In the bottom right corner, the photograph of a real device is shown. (c) Cycling stability of a supercapacitor showing a capacitance retention of 96% after 10 000 cycles. The graph in the inset corresponds to a set of charge/discharge cycles, which shows a highly stable performance. Reproduced with permission from ref. 113. Copyright 2016 Wiley-VCH Verlag GmbH & Co. KGaA, Weinheim.

with/without added active materials to form a composite in the last few years are represented, together with the used laser system and conditions, the device performance and the corresponding references. We have ordered the electrodes in chronological order to track the evolution of the electrodes over time.

### 2.3 Microelectrodes

Microsupercapacitors (MSCs) are miniaturized supercapacitor devices. Compared to standard supercapacitors, MSCs use the same graphene-based materials and electrolytes, and include the same components; their performance can also be enhanced by the use of pseudocapacitive elements and their working principle is unchanged, while the scale is greatly reduced. This change in size comes not only in the in-plane dimensions, but more importantly in the out-of-plane one, its thickness. MSCs are thin-film, planar devices, a characteristic that allows them to

be integrated much more easily in a variety of applications and processes, including flexible and wearable devices<sup>63</sup> or placed alongside silicon using the same CMOS-compatible processes for on-chip energy storage.<sup>151</sup>

While standard supercapacitors use sandwiched/stacked parallel electrodes in planar or rolled-up configurations for coin-like cells, MSCs are typically designed as interdigitated electrodes (IDEs), since this configuration presents several advantages over stacked ones. Fig. 8a depicts the comparison between the traditional sandwich (top) and the IDE (bottom) geometries.<sup>22</sup> In Fig. 8b, the ion transport in both device geometries is compared as well.<sup>22</sup> This interdigitated design is used because it provides two clear advantages, while also adding some challenges. First, it allows processing the full device on the same surface, eliminating the need for an extra assembly step, which is key for being integrated into Si-based CMOS processes on an industrial scale. It is also beneficial for ionic transport, as the perimeter of both electrodes is maximized with the number of fingers and provides a better contact and accessibility for the electrolyte. Structuring the electrode in fingers shortens ion diffusion paths, which allows for better rate performance and enables the use of certain materials that would have poor electrolyte infiltration if used in bulk. It also avoids the need of using a separator, as both electrodes are separated in-plane by a controllable gap, adding new possibilities to the design and optimization of these structures to maximize the performance. The main challenge, however, is the need to define the designed geometry for all the layers of the device, from the current collectors to the active material. This can be done through standard lithography and etching processes or through other less conventional methods, including laser ablation,<sup>152–158</sup> mask-assisted filtration,<sup>159–162</sup> screen printing,<sup>163,164</sup> extrusion printing,<sup>165</sup> electrodeposition<sup>156,166,167</sup> and others.

Typically, current collectors are fabricated by lithography, by means of photoresist layer deposition, metal evaporation/sputtering and lift-off. This allows transferring the interdigitated design from an optical mask to the sample and can be done on different substrates depending on the final application. Differences arise from the deposition of the electrode materials, which are conductive porous carbons that also need to be geometrically defined. Starting from a dispersion contained in a solvent, deposition and filtration through a hard mask can create such electrodes, the limitation being the size control and resolution of this physical hard mask that needs to be machined or 3D printed. Screen printing or doctor blade coating can also be used, though they share the same limitation. Chemical vapor deposition allows depositing graphene materials from gaseous carbon precursors onto a substrate at a very high temperature and offers great control over the porosity and microstructure, and even more if plasma is added to the chamber. The huge number of parameters that can be tuned makes it a very versatile but complex process, which in most cases needs extra steps to eliminate carbon materials from the surface, as the deposition occurs in the whole surface of the substrate. Electrodeposition can also be used to form porous and conductive electrodes from graphene materials in solution, and it is also



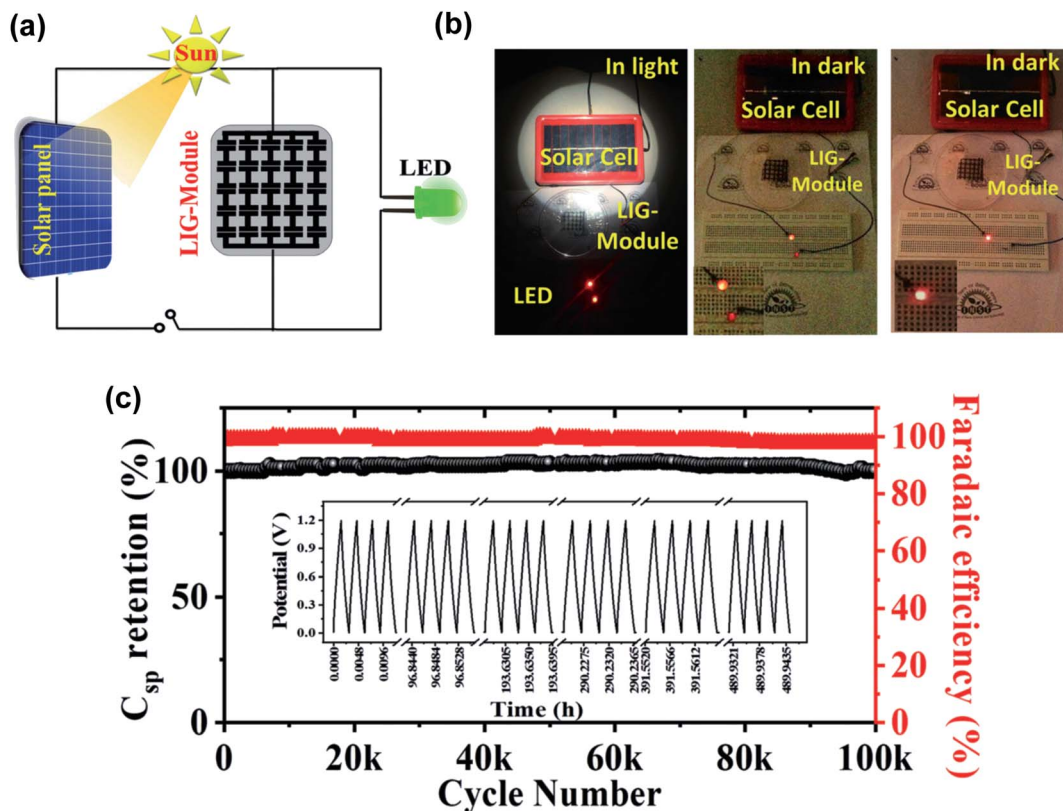


Fig. 7 (a) Schematic drawing of a circuit including an energy storage element (based on LIG microsupercapacitors), a solar panel and an LED. (b) Labeled pictures showing the working elements of this circuit. (c) Graph showing the galvanostatic charge–discharge cycling test for the microsupercapacitor module, keeping an outstanding capacitance retention for up to 100k cycles. Reproduced with permission from ref. 149. Copyright 2019 Royal Society of Chemistry.

a common method to deposit pseudocapacitive elements, facilitating the production of hybrid and asymmetric devices.

Some of these carbon materials can be used as-assembled, due to their good properties regarding conductivity, porosity and geometry definition, while others such as graphene oxide, a very common and accessible graphene material, need to be further processed. Graphene oxide in this case can be reduced

chemically or thermally. Direct laser writing appears as a very versatile technique which can be used to synthesize new graphene materials (a) from polymers, as is the case of LIG,<sup>112</sup> (b) by processing GO into LrGO<sup>58</sup> and (c) by even processing pseudocapacitive elements, for example, modifying manganese acetate into MnO<sub>2</sub>.<sup>168</sup> Furthermore, it can also be used to define the electrode geometry in a very precise and controlled way. When

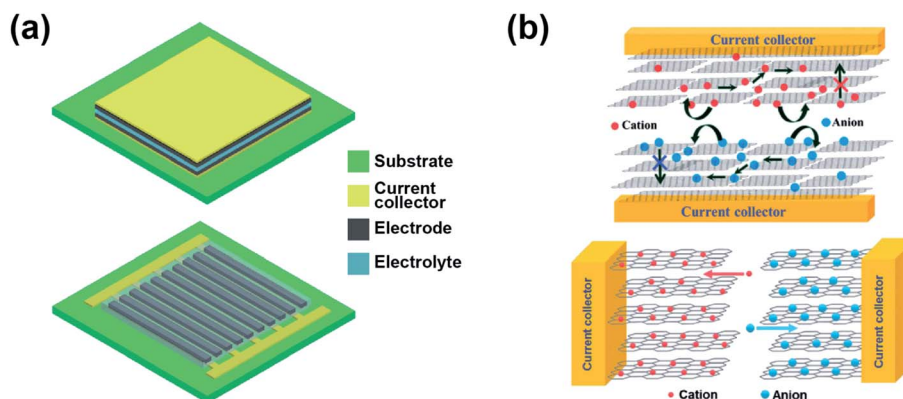


Fig. 8 Schematic drawing of (a) two assembled microsupercapacitors (MSCs) with sandwich (top) and interdigitated (bottom) geometries, and of (b) the ion transport at the nanometric scale in both configurations: sandwich (top) and interdigitated (bottom) geometries. Reproduced with permission from ref. 22. Copyright 2014 Royal Society of Chemistry.

a laser is used to define the geometry of a previously processed material, the process will be referred to as 'laser ablation' or 'laser etching', while 'laser processing' will be used to refer to processes where the laser modifies the active electrode materials, such as LrGO or LIG.

Tiliakos *et al.*<sup>169</sup> explored in 2018 the versatility of the DLW technique in order to create increasingly intricate fractal architectures which increased the perimeter of electrodes for better electrolyte accessibility, achieving  $6.1 \text{ mF cm}^{-2}$ . In order to increase the performance of these devices, pseudocapacitive elements are added. Using environmentally friendly biomass as a precursor, Zhang *et al.*<sup>119</sup> fabricated MSCs from a lignin/PVA film. The porous laser scribed lignin device achieved a surprising  $25 \text{ mF cm}^{-2}$  capacitance with a high power density of  $8 \text{ mW cm}^{-2}$  and energy density of  $4 \mu\text{W h cm}^{-2}$ . Wu *et al.*<sup>170</sup> grew selectively, by solvothermal synthesis, conductive 2D metal-organic framework (MOF) structures on a LIG substrate, which acts also as the current collector in these MSCs, getting an areal capacitance of  $15.2 \text{ mF cm}^{-2}$  and a decent energy density of  $4.1 \mu\text{W h cm}^{-2}$  at a high-power density of  $7 \text{ mW cm}^{-2}$ . Similarly, but with a simpler approach, Bhattacharya *et al.*<sup>171</sup> used a LIG interdigitated MSC and enhanced its performance with 'red mud', a mining by-product containing metallic oxides, known to be good pseudocapacitive elements. By simple dip-coating, the capacitance reached  $203 \text{ mF cm}^{-2}$  at  $0.1 \text{ mA cm}^{-2}$ , with an energy density of  $18 \mu\text{W h cm}^{-2}$  at  $0.66 \text{ mW cm}^{-2}$ . It is important to highlight the work of Yu *et al.*,<sup>172</sup> in which a commercial PI film was modified to make it more sensitive to a laser and achieve thicker 3D LIG frameworks of up to  $320 \mu\text{m}$ . Adding a high mass loading of pseudocapacitive polypyrrole, the devices reached a very high energy density of  $134.4 \mu\text{W h cm}^{-2}$  at  $0.3 \text{ mW cm}^{-2}$ , with a great cycling stability of 95.6% at  $2.5 \text{ mA cm}^{-2}$  after 10 000 cycles.

Direct laser writing can also be used to process and transform not only substrates, but also pseudocapacitive elements. Zhu *et al.*<sup>168</sup> fabricated a LIG MSC from PEEK, a technical polymer, and afterwards deposited on top of a solution of manganese acetate, transforming it into  $\text{MnO}_2$  by a second pass of the laser. This electrode showed a high capacitance of  $49 \text{ mF cm}^{-2}$  and the symmetric MSC delivered a maximum energy density of  $3.1 \mu\text{W h cm}^{-2}$  and a power density of  $2.5 \text{ mW cm}^{-2}$ . Following a similar approach but condensing the two laser irradiations into one, Liu *et al.*<sup>173</sup> and Xu *et al.*<sup>174</sup> pre-treated a polyimide film with metallic precursors, which became metallic oxides at the same time as the polymer transformed into LIG. An  $\text{Fe}_3\text{O}_4$  NP decorated LIG MSC achieved an outstanding capacitance of  $719 \text{ mF cm}^{-2}$ , and an energy density of  $60.2 \mu\text{W h cm}^{-2}$  at  $0.3 \text{ mW cm}^{-2}$  power density,<sup>173</sup> while LIG with  $\text{Co}_3\text{O}_4$  achieved a much higher energy density of  $286.38 \mu\text{W h cm}^{-2}$  at a similar power.<sup>174</sup> However, the achieved capacitance was much smaller,  $1.9 \text{ mF cm}^{-2}$ .

Regarding the application of DLW to reduce GO and fabricate LrGO MSCs, Shen *et al.*<sup>175</sup> used a femtosecond laser to define interdigitated LrGO regions with ultra-short spacing, reaching  $6.3 \text{ mF cm}^{-2}$  after accurately applying a gel electrolyte by laser-induced micro-droplet transfer. In a single step, Gholami *et al.*<sup>133</sup> laser reduced a mixture of GO and PANI after

having used a hard mask to define the IDE geometry of the drop cast slurry, achieving  $72 \text{ mF cm}^{-2}$  and a decent cycling stability of 93.5% at  $0.7 \text{ mA cm}^{-2}$  after 1000 cycles, which is still challenging for conductive polymers.

Using a hard mask to define the geometry of the device, both for contacts and active materials, is a very valid, scalable and useful method to fabricate MSCs. Couly *et al.*<sup>160</sup> spray coated rGO and MXenes on a flexible substrate using a hard mask, showing that the IDE geometry achieved had better power performance than its sandwiched counterpart. Chih *et al.*<sup>164</sup> used a screen printing method to deposit electrochemically exfoliated graphene and CNTs into IDEs and after adding a gel electrolyte achieved  $7.7 \text{ mF cm}^{-2}$ , with an excellent cycling stability >99% at  $200 \text{ mV s}^{-1}$  after 15 000 cycles. Functionalizing chemically graphene in solution was the approach used by Zhou *et al.*,<sup>159</sup> who filtered through a mask a solution of fluorine-doped electrochemically exfoliated graphene, which increased the capacitance of the device up to  $17.4 \text{ mF cm}^{-2}$  and reached an energy density and power density of  $7.67 \mu\text{W h cm}^{-2}$  and  $2.73 \text{ mW cm}^{-2}$ , respectively. Again, using mask-assisted filtration, Xiao *et al.*<sup>161</sup> fabricated MSCs made of exfoliated graphene, CNTs and PEDOT:PSS, on top of a pre-stretched substrate, which ensured good conductivity and porosity after relaxation. The device reached an exceptional capacitance of  $107 \text{ mF cm}^{-2}$ .

For the cases where hard masks were not used to define the geometry of these devices, laser etching arises as a versatile technique for research, as it allows quick modification of the design for optimization and rapid prototyping. In general, laser etched devices achieve very good electrochemical properties as the focus can be kept on optimizing the material, regardless of the future interdigitated geometry that will be applied. Shao *et al.*<sup>152</sup> prepared a thin film of 3D cellular graphene which after laser ablation reached  $2.7 \text{ mF cm}^{-2}$  but with a high-power performance of  $5.3 \text{ mW cm}^{-2}$ . By patterning several CVD graphene monolayers *via* laser etching, Ye *et al.*<sup>155</sup> could exploit the edge effects of the geometry and achieved  $2.8 \text{ mF cm}^{-2}$  by adding PANI to the device. They also used their device to demonstrate an integrated energy harvesting sensor platform. Similarly, Yoo *et al.*<sup>154</sup> also exploited the edge effects of patterned heat-treated graphene oxide to fabricate a MSC with  $40 \text{ mF cm}^{-2}$  and an energy density of  $5.4 \mu\text{W h cm}^{-2}$ , outstanding values taking into account that no pseudocapacitive elements were added. By compositing an rGO film with polypyrrole and sputtering Au nanoparticles on top to ensure a good contact, Purkait *et al.*<sup>156</sup> reached an energy density of  $11.82 \mu\text{W h cm}^{-2}$  and a power density of  $2.36 \text{ mW cm}^{-2}$ . By using ionic liquid electrolytes and increasing the voltage window up to 3 V, Gao *et al.*<sup>157</sup> produced an outstanding laser etched rGO supercapacitor with an energy density of  $32 \mu\text{W h cm}^{-2}$  at a power density of  $1 \text{ mW cm}^{-2}$ .

Alternative techniques are always being developed,<sup>176,177</sup> and the MSC field is growing constantly. By interference lithography, Kim *et al.*<sup>178</sup> patterned a photoresistive polymer, which after development and carbonization formed a conductive solid backbone with patterned pores for excellent electrolyte accessibility. In fact, the fabricated thick interdigitated MSC shows an outstanding power density of  $165 \text{ mW cm}^{-2}$ , with a high



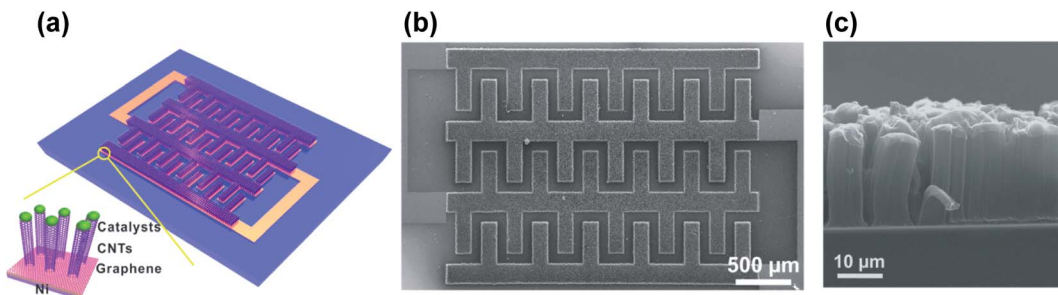


Fig. 9 (a) Schematic structure of a graphene-CNT MSC, grown on a Si substrate by chemical vapor deposition, with an inset showing the catalyst nanoparticles. (b) SEM image of the fabricated MSC, top view. (c) Cross-sectional SEM image of the graphene/CNT supercapacitor grown on a Ni catalyst/metal electrode. Reproduced with permission from ref. 180. Copyright 2012 American Chemical Society.

energy density of  $17.75 \mu\text{W h cm}^{-2}$ . Using MEMS-based Si etching techniques to provide a 3D support for capacitive carbon materials, as Li *et al.* proposed,<sup>179</sup> the fabricated supercapacitor reached remarkably high energy and power densities of  $15.1 \mu\text{W h cm}^{-2}$  and  $2.45 \text{ mW cm}^{-2}$  respectively, due to a high  $\text{RuO}_x$  loading and an improved hierarchical carbon microstructure on Si. Fig. 9 show an example of a hierachic graphene/CNT-based MSC composite produced on a Si/SiO<sub>2</sub> substrate.<sup>180</sup> This composite was grown directly by CVD from Ni interdigitated electrodes fabricated on the Si layer by conventional photolithography. In Fig. 9a, the scheme of the device design is shown. Fig. 9b shows a SEM image of a fabricated MSC and Fig. 9c a cross-sectional SEM image of the graphene/CNT structure, grown on a Ni catalyst/electrode layer by CVD.

MSCs were initially proposed to be integrated on-chip in Si-based platforms, using the CMOS technology for mass production.<sup>181</sup> However, motivated by the rise of wearable technology, new improvements have emerged based on flexible, stretchable and bendable substrates. Thus, many of the techniques developed recently to fabricate MSCs have been applied to add a flexibility component to the performance of the device.<sup>35</sup> Together with gel-based, quasi-solid-state, and solid-state electrolytes, these devices have demonstrated to keep their performance after cyclability bending stress tests over

a large number of cycles. In Fig. 10a, several photographs show the bending of a supercapacitor at different angles.<sup>163</sup> The cyclic voltammograms shown in Fig. 10b, taken at different bending states, show that the rectangular shape is kept regardless of the bending angle of the device. The capacitance retention under the different bending angles is also complete, compared to the value in the flat state.<sup>163</sup> These developments pave the way for flexible supercapacitors as energy storage elements that can be easily integrated into wearable electronics.

To conclude this section, we provide Table 3, where MSCs synthesized by different processes and with/without added active materials to form a composite in the last few years are represented, together with the device performance and the corresponding references. We have ordered the MSCs in chronological order to track the trend over time.

### 3 Results and discussion: Ragone plots of the latest graphene-based supercapacitors

Graphene supercapacitors are rapidly evolving from laboratory prototypes to final devices that will complement or even perhaps compete with commercial batteries in the near future. This is because their properties and performance have greatly

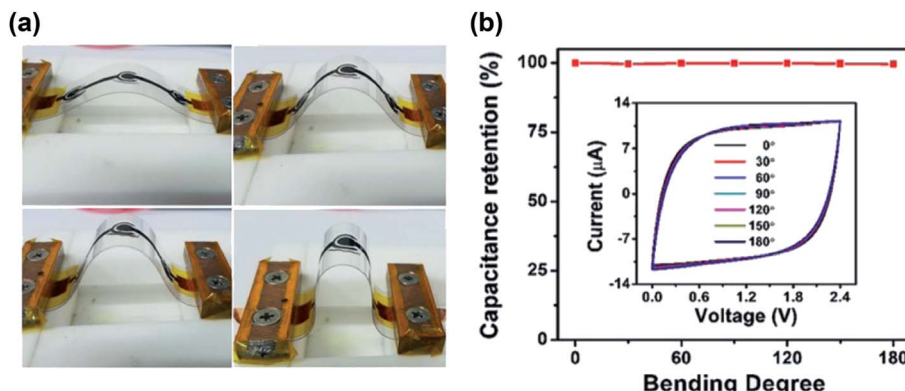


Fig. 10 (a) Photographs of the bending cycle of a flexible microsupercapacitor at different angles. (b) Capacitance retention graph across several bending angles. The inset shows the cyclic voltammetry curves of the device at those angles, showing a very stable performance. Reproduced with permission from ref. 163. Copyright 2019 Royal Society of Chemistry.





Table 3 Summary of MScs

Synthesis method	Active materials	Capacitance ( $\text{mF cm}^{-2}$ )	Energy density ( $\mu\text{Wh cm}^{-2}$ )	Power density ( $\text{mW cm}^{-2}$ )	Retention (%) after a number of cycles	Year	Ref.	
Spray coating through a mask	rGO and $\text{Ti}_3\text{C}_2\text{T}_x$	2.4 at 2 $\text{mV s}^{-1}$	0.26	0.01	97% after 10 000 at 0.2 $\text{mA cm}^{-2}$	2017	160	
Freeze-casting assisted infiltration assembly method and laser ablation	Cellular graphene	2.47 at 5 $\text{mV s}^{-1}$	0.34	5.3	97.6% after 10 000 at 1 $\text{mA cm}^{-2}$	2017	152	
Electrodeposition	rGO and $\text{MnO}_x$	1.63 at 0.3 $\text{mA cm}^{-2}$	0.27	0.19	85% after 1000	2018	166	
Electrodeposition and laser ablation	rGO, PPY and nanoporous Au	29.21 at 0.07 $\text{mA cm}^{-2}$	11.72	2.36	85.9% after 10 000 at 5 $\text{mA cm}^{-2}$	2018	156	
MPECVD* and Si-based microfabrication techniques	Graphene nanowall and $\text{RuO}_2$	109 at 5 $\text{mV s}^{-1}$	15.10	2.49	90.2% after 3000 at 50 $\text{mV s}^{-1}$	2018	179	
Screen-printing with graphene ink	Screen-printed graphene	0.89 at 5 $\text{mV s}^{-1}$	0.91	0.15	91.8% after 10 000 at 0.2 $\text{mA cm}^{-2}$	2018	163	
DLW	LIG	25.1 at 0.05 $\text{mA cm}^{-2}$	4	8	98.5% after 12 000 at 2 $\text{mA cm}^{-2}$	2018	119	
Interference lithography and plasma etching	Boron-doped porous carbon	7.15 at 100 $\text{mV s}^{-1}$	17.75	165	85% after 12 000 at 5000 $\text{mV s}^{-1}$	2018	178	
Mask-assisted filtration of ink	Fluorine doped graphene	17.4 at 1 $\text{mV s}^{-1}$	7.67	2.73	93% after 5000	2018	159	
DLW	LIG	6.1 at 20 $\text{mV s}^{-1}$	0.96	0.25	—	2018	169	
CVD and laser ablation	Graphene	45.2 at 10 $\text{mV s}^{-1}$	0.04	3.17	—	2018	155	
Mask-assisted filtration of ink	Graphene, CNTs and PEDOT	107.5 at 5 $\text{mV s}^{-1}$	1.27	0.12	—	2018	161	
DLW	LrGO	6.3 at 1 $\text{mV s}^{-1}$	0.09	0.60	100% after 1000 at 500 $\text{mV s}^{-1}$	2018	175	
Biomimetic microfluidic fabrication	rGO and metallic $\text{MoS}_2$ microfibers	48.4 at 1 $\text{V s}^{-1}$	4	0.42	0.00	97% after 10 000	2018	176
Conventional lithographic techniques and laser ablation	rGO	40 at 10 $\text{mV s}^{-1}$	5.40	1.48	83.5% after 10 000 at 100 $\text{mV s}^{-1}$	2018	154	
Freeze-drying and laser ablation	rGO and $\text{Ti}_3\text{C}_2\text{T}_x$ aerogel	34.6 at 1 $\text{mV s}^{-1}$	2.18	0.06	91% after 15 000 at 2 $\text{mA cm}^{-2}$	2018	153	
Ion-liquid reduction and laser ablation	rGO and carbon paper	27.4 at 0.7 $\text{mA cm}^{-2}$	32.10	1.05	—	2019	157	
Screen-printing	Graphene and CNTs	7.7 at 5 $\text{mV s}^{-1}$	1.07	1.65	> 99% after 15 000 at 200 $\text{mV s}^{-1}$	2019	164	
DLW	LIG and Ni-catecholate MOF***	15.2 at 0.2 $\text{mA cm}^{-2}$	4.1	0.32	87% after 5000 at 2 $\text{mA cm}^{-2}$	2019	170	
Slurry coating and laser ablation. Electrodeposition.	n-doped graphene and $\text{MnO}_2$	13.3 at 0.25 $\text{mA cm}^{-2}$	5.88	1.13	84% after 5000 at 2 $\text{A g}^{-1}$	2019	158	
DLW	LIG and $\text{MnO}_2$	48.9 at 10 $\text{mV s}^{-1}$	3.1	2.5	94.3% after 3000 at 0.5 $\text{mA cm}^{-2}$	2020	168	
DLW	LIG and $\text{Fe}_3\text{O}_4$ nanoparticles	719.28 at 1 $\text{mV s}^{-1}$	60.2	0.3	74% after 900 at 20 $\text{mV s}^{-1}$	2020	173	
DLW	LIG and $\text{Co}_3\text{O}_4$	10.9 at 5 $\text{mV s}^{-1}$	286.38	0.75	97.8% after 10 000 at 0.08 $\text{mA cm}^{-2}$	2020	174	
DLW	LIG and PPY	2412.2 at 0.5 $\text{mA cm}^{-2}$	10.94	0.43	95.6% after 10 000 at 2.5 $\text{mA cm}^{-2}$	2020	172	
DLW	LIG and red-mud	203 at 0.1 $\text{mA cm}^{-2}$	134.4	0.325	81% 4000 at 0.3 $\text{mA cm}^{-2}$	2020	171	
Drop casting over carbon fiber. Electrodeposition	rGO, PEDOT:PSS and $\text{MnO}_2$	550 at 3 $\text{mA cm}^{-2}$	18	0.66	95% after 5000 at 12 $\text{mA cm}^{-2}$	2020	167	
Mask-assisted deposition	EG + CNT + rGO/PPY	38 at 1 $\text{mV s}^{-1}$	2	1.36	82% after 4500	2020	162	
Slurry coating on an imprinted substrate	GO, graphene aerogel and $\text{MnO}_2$	14.2 at 10 $\text{mV s}^{-1}$	150	14.1	85% after 25 000	2020	177	

improved over the last decade. The three technologies that have contributed the most to their development, namely, graphene foam, laser reduction and microsupercapacitors, have been reviewed in detail and are summarized below.

Graphene foam made by CVD from sacrificial templates enables making high capacity electrodes for large area supercapacitors, with a demonstrated gravimetric capacitance of up to  $2585 \text{ F g}^{-1}$  (ref. 100) and a capacitance retention of 96.5% after 10 000 cycles.<sup>90</sup> Graphene provides high electrical conductivity and its porous structure presents a large surface area and allows an easy transit of electrolyte ions. In this way, a light and flexible 3D electrode can be obtained. DLW represents a low-cost, fast, and single step technique to produce large area and flexible electrodes based on laser reduced GO or laser induced graphene. Despite achieving electrodes with very good capacitance retention (see Table 2), the laser wavelength and processing parameters required to produce supercapacitors with higher specific capacitance than those using graphene foam fabricated by CVD have not been optimized yet. All these graphene forms, namely, graphene foam, LrGO and LIG, have an empty pore area that can be functionalized with various pseudocapacitive materials. The most widely used so far are metallic oxides and conductive polymers, although recently

transition metal sulfides are being explored to push further the achievable power density, cycling stability and operating voltage window.

Miniaturized supercapacitors, or MSCs, are becoming increasingly popular due to their integration possibilities. The rise of wearable electronics is driving this approach to grow rapidly, and scaling down the supercapacitor technology to the microscale has revealed some advantages. The use of IDEs eases ion accessibility, improving power performance, and gel and solid-state electrolytes allow these devices to be easily encapsulated in bendable or stretchable modules. Electrodes can be fabricated by scalable, cheap and quick processes such as screen printing or drop casting, and can be grown on top of or transferred to almost any target substrate. Laser writing has emerged recently as a quick and easy way to fabricate supercapacitor electrodes from inexpensive materials and to pattern them easily into interdigitated microsupercapacitor electrodes. This flexibility is ideal for their integration into the growing industry of wearable electronics, where MSCs are expected to play a crucial role in the future.

As the Ragone plot in Fig. 11a shows, the energy and power density of new supercapacitor devices are already approaching energy density performances that were typically restricted to

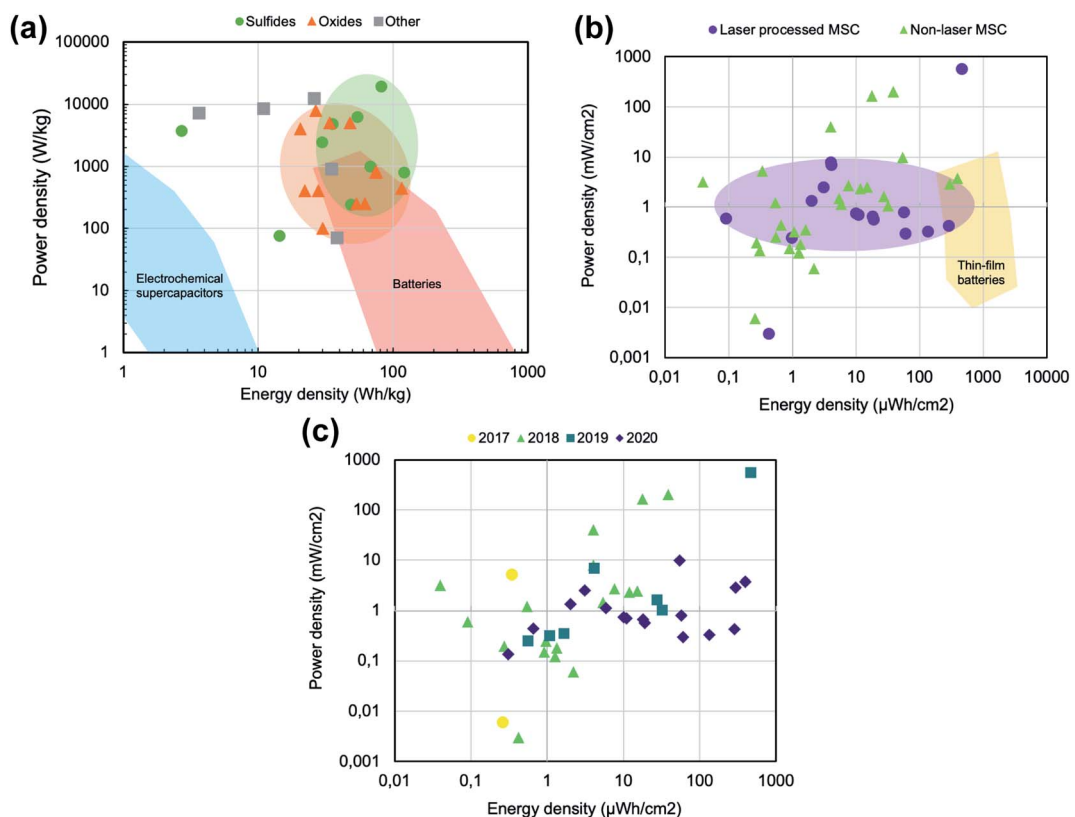


Fig. 11 (a) Schematic gravimetric Ragone plot where the typical working regions for commercial supercapacitors and batteries are highlighted. Each dot represents one working point of a graphene-foam based device classified by the type of its active pseudocapacitive material, green for sulfides, orange for oxides and grey for other compounds, such as metal hydroxides or metallic nanoparticles. (b) Schematic areal Ragone plot. Each dot represents one thin-film device reported in the literature, purple for laser processed micro-supercapacitors and green for non-laser microsupercapacitors. The yellow region represents the typical working point of thin-film batteries as reported by ref. 182. (c) Schematic areal Ragone plot of the same data used in Fig. 11b, classified by the publishing date.

batteries, but with better power performance. Each dot in this graph represents an energy-power working point of the fabricated devices included in Table 1. Most of these devices have been fabricated using graphene foam of CVD graphene or rGO, but are always complemented with pseudocapacitive elements. CVD graphene shows a more open-pore interconnected network and is of very high quality, while several key properties depend to great extent on the metallic foam template on which it is grown, such as the surface area, or the pore size and distribution. On the other hand, rGO typically creates compact 3D porous structures with smaller pores and a higher surface area, while being less accessible to the electrolyte and having worse electrical properties than CVD graphene. However, our comparison shows that both CVD graphene and rGO are very competitive materials for the fabrication of supercapacitor devices, showing comparable results in the Ragone plot shown in Fig. 11a. However, differences regarding the pseudocapacitive elements included in these devices are more clearly highlighted in that same graph. The recent literature has reported a large number of devices that use, in order to achieve the best performance, mostly bimetallic oxides and sulfides, as well as other materials including hydroxides, as pseudocapacitive elements. The use of metallic and bimetallic sulfides (green dots) has been showing the best results when compared to their oxide counterpart (orange triangles), and these devices show already a comparable, if not better, working point to that stated by Simon and Gogotsi for batteries in their recent review of the field.<sup>5</sup> It is important to note that the red area of Fig. 11a and the blue area, taken from the Simon and Gogotsi article, only include commercial devices, and the dots are exclusively plotted from the data of research papers published during the last 3 years. This shows the strength of the supercapacitor technology, which can not only complement, but also compete directly with batteries regarding energy density and power density, showing much better cycling stabilities and being fabricated from materials less scarce than lithium.

This gravimetric classification includes graphene foam-based devices, which typically are reported using per-kg metrics. However, for thin film devices such as microsupercapacitors, figures-of-merit are typically given in areal or volumetric terms, as they are fabricated with thicknesses in the range of a few  $\mu\text{m}$ . Its mass is not really the defining factor limiting its performance, but its area. Fig. 11b shows this classification in an areal Ragone plot, where every dot represents one energy-power working point of a fabricated microsupercapacitor device as reported in the literature (references shown in Tables 2 and 3). There is growing interest in laser processing technology, due to its multiple advantages regarding flexibility, speed and low-cost. In the past two years, the number of papers published using laser writing to process supercapacitor materials has grown a lot, almost monopolizing all recent research in the field. Most of the papers found in the literature which used non-laser processes to fabricate microsupercapacitors were mostly published in 2018 and before, using techniques such as mask-assisted filtration, screen printing or standard lithography to define the interdigitated geometries. However, from 2019, mostly laser-processed

microsupercapacitors have been found. This classification of the results by year can be seen in Fig. 11c.

Regarding electrochemical performance, and despite all this recent interest, laser processed MSCs, shown as purple dots in Fig. 11b, show a saturation of the power density in the  $10 \text{ mW cm}^{-2}$  range, going even lower for the most energy dense performances, towards the  $1 \text{ mW cm}^{-2}$  limit. This could be due to the lower quality of the materials that can be achieved through laser processing, be it laser induced graphene from polymeric films or laser-reduced graphene oxide from graphene oxide films. However, the energy density of these devices has been steadily increasing since 2017, and some recent devices lay in a working range very close to that of thin film batteries, devices comparable to microsupercapacitors in their metrics. By compositing these laser-processed graphene materials with pseudocapacitive elements, for example  $\text{Co}_3\text{O}_4$  (ref. 174) or  $\text{Fe}_3\text{O}_4$  (ref. 173), the energy density is being pushed towards the thin film battery region, which are the best performing devices in terms of areal energy density nowadays.<sup>182</sup>

## 4 Conclusion and outlook

In summary, to move the supercapacitor and MSC field forward, DLW processing has recently emerged as a very promising technique. This technique allows quick, one-step processing to create a highly porous and conductive 3D network of graphene sheets, using commercial laser systems. Building up from technologies such as 3D printers and laser cutters, these systems demonstrate great scalability and increasing precision, as well as industrial availability. Furthermore, structuring these materials into IDEs helps electrolyte accessibility and could allow for better power performance. However, most of the recent work in the field has focused on increasing its energy density towards the thin-film battery range, and it will be a challenge for the following years to further increase the power density. On top of this, synergies are appearing and can be exploited, as some studies suggest the advantages of using laser processing for both the graphene material and the pseudocapacitive element. This combined process can, for example, add oxygen vacancies to metal oxides or transform through photo-chemistry conductive polymers, which could be used together with graphene materials fabricated using new laser 3D printer systems. However, there are still some challenges that need to be overcome for the widespread use of graphene-based supercapacitors. First, the large-scale fabrication of porous graphene materials with high quality and uniformity must be ensured. Optimization is still needed in several areas, such as the intimate contact and adherence of pseudocapacitive elements on the graphene network, or the choice of an ideal pseudocapacitive material and its possible synergies with the electrolyte for an optimized voltage window and cyclability. Minimizing the agglomeration and restacking of the graphene sheets is a problem present in all-carbon EDLCs that must be addressed, while in the case of pseudocapacitors, it can be done by intercalating the graphene material with active nanoparticles.

If the expectations are met, graphene supercapacitors and microsupercapacitors are meant to become a competitive



complement, or even alternative, to traditional lithium ion batteries and thin film batteries, as well as an essential component in new wearable and portable electronic devices.

## Conflicts of interest

There are no conflicts of interest to declare.

## Acknowledgements

A. Velasco is in receipt of an FPU grant from the Spanish Government. This work was supported by Spanish Ministerio de Economía y Competitividad (MINECO), project DIGRAFEN (ENE2017-88065-C2-1-R) (MINECO/AEI/FEDER, UE) and from the Comunidad de Madrid through project NMAT2D-CM (P2018/NMT-4511). J. Pedrós acknowledges financial support from MINECO (Grant RyC-2015-18968) and UPM (Ayuda para la incorporación y retención de talento doctor, Programa Propio de I+D+i 2019 y 2020).

## References

- 1 R. Kotz and M. Carlen, *Electrochim. Acta*, 2000, **45**, 2483–2498.
- 2 M. Winter and R. J. Brodd, *Chem. Rev.*, 2004, **104**, 4245–4269.
- 3 J. Yan, Q. Wang, T. Wei and Z. Fan, *Adv. Energy Mater.*, 2014, **4**(4), 1300816.
- 4 P. Simon, Y. Gogotsi and B. Dunn, *Science*, 2014, **343**, 1210–1211.
- 5 P. Simon and Y. Gogotsi, *Nat. Mater.*, 2020, **19**, 1151–1163.
- 6 Z. Lin, E. Goikolea, A. Balducci, K. Naoi, P. L. Taberna, M. Salanne, G. Yushin and P. Simon, *Mater. Today*, 2018, **21**, 419–436.
- 7 L. Kouchachvili, W. Yaici and E. Entchev, *J. Power Sources*, 2018, **374**, 237–248.
- 8 X. Dai, F. Wan, L. Zhang, H. Cao and Z. Niu, *Energy Storage Mater.*, 2019, **17**, 143–150.
- 9 D. P. Dubal, N. R. Chodankar, D. H. Kim and P. Gomez-Romero, *Chem. Soc. Rev.*, 2018, **47**, 2065–2129.
- 10 X. Chen, N. S. Villa, Y. Zhuang, L. Chen, T. Wang, Z. Li and T. Kong, *Adv. Energy Mater.*, 2020, **10**, 1902769.
- 11 Q. Zhang, J. Sun, Z. Pan, J. Zhang, J. Zhao, X. Wang, C. Zhang, Y. Yao, W. Lu, Q. Li, Y. Zhang and Z. Zhang, *Nano Energy*, 2017, **39**, 219–228.
- 12 Q. Zhang, W. Xu, J. Sun, Z. Pan, J. Zhao, X. Wang, J. Zhang, P. Man, J. Guo, Z. Zhou, B. He, Z. Zhang, Q. Li, Y. Zhang, L. Xu and Y. Yao, *Nano Lett.*, 2017, **17**, 7552–7560.
- 13 Z. Zhou, Q. Zhang, J. Sun, B. He, J. Guo, Q. Li, C. Li, L. Xie and Y. Yao, *ACS Nano*, 2018, **12**, 9333–9341.
- 14 K. B. Oldham, *J. Electroanal. Chem.*, 2008, **613**, 131–138.
- 15 B. E. Conway, *Electrochemical Supercapacitors: Scientific Fundamentals and Technological Applications*, Springer US, 1st edn.
- 16 Q. Meng, K. Cai, Y. Chen and L. Chen, *Nano Energy*, 2017, **36**, 268–285.
- 17 Y. Jiang and J. Liu, *Energy Environ. Mater.*, 2019, **2**, 30–37.
- 18 B. Pal, S. Yang, S. Ramesh, V. Thangadurai and R. Jose, *Nanoscale Adv.*, 2019, **1**, 3807–3835.
- 19 C. Zhong, Y. Deng, W. Hu, J. Qiao, L. Zhang and J. Zhang, *Chem. Soc. Rev.*, 2015, **44**, 7484–7539.
- 20 M. D. Stoller and R. S. Ruoff, *Energy Environ. Sci.*, 2010, **3**, 1294–1301.
- 21 A. Noori, M. F. El-Kady, M. S. Rahamanifar, R. B. Kaner and M. F. Mousavi, *Chem. Soc. Rev.*, 2019, **48**, 1272–1341.
- 22 M. Beidaghi and Y. Gogotsi, *Energy Environ. Sci.*, 2014, **7**, 867–884.
- 23 H. Li, C. Qi, Y. Tao, H. Liu, D. W. Wang, F. Li, Q. H. Yang and H. M. Cheng, *Adv. Energy Mater.*, 2019, **9**, 1900079.
- 24 C. Backes, A. M. Abdelkader, C. Alonso, A. Andrieux-Ledier, R. Arenal, J. Azpeitia, N. Balakrishnan, L. Banszerus, J. Barjon, R. Bartali, S. Bellani, C. Berger, R. Berger, M. M. B. Ortega, C. Bernard, P. H. Beton, A. Beyer, A. Bianco, P. Bøggild, F. Bonaccorso, G. B. Barin, C. Botas, R. A. Bueno, D. Carriazo, A. Castellanos-Gomez, M. Christian, A. Ciesielski, T. Ciuk, M. T. Cole, J. Coleman, C. Coletti, L. Crema, H. Cun, D. Dasler, D. De Fazio, N. Díez, S. Drieschner, G. S. Duesberg, R. Fasel, X. Feng, A. Fina, S. Forti, C. Galotis, G. Garberoglio, J. M. García, J. A. Garrido, M. Gibertini, A. Gölzhäuser, J. Gómez, T. Greber, F. Hauke, A. Hemmi, I. Hernandez-Rodriguez, A. Hirsch, S. A. Hodge, Y. Huttel, P. U. Jepsen, I. Jimenez, U. Kaiser, T. Kaplas, H. K. Kim, A. Kis, K. Papagelis, K. Kostarelos, A. Krajewska, K. Lee, C. Li, H. Lipsanen, A. Liscio, M. R. Lohe, A. Loiseau, L. Lombardi, M. F. López, O. Martin, C. Martín, L. Martínez, J. A. Martin-Gago, J. I. Martínez, N. Marzari, Á. Mayoral, J. McManus, M. Melucci, J. Méndez, C. Merino, P. Merino, A. P. Meyer, E. Minuissi, V. Miseikis, N. Mishra, V. Morandi, C. Munuera, R. Muñoz, H. Nolan, L. Ortolani, A. K. Ott, I. Palacio, V. Palermo, J. Parthenios, I. Pasternak, A. Patane, M. Prato, H. Prevost, V. Prudkovskiy, N. Pugno, T. Rojo, A. Rossi, P. Ruffieux, P. Samorì, L. Schué, E. Setijadi, T. Seyller, G. Speranza, C. Stampfer, I. Stenger, W. Strupinski, Y. Svirko, S. Taioli, K. B. K. Teo, M. Testi, F. Tomarchio, M. Tortello, E. Treossi, A. Turchanin, E. Vazquez, E. Villaro, P. R. Whelan, Z. Xia, R. Yakimova, S. Yang, G. R. Yazdi, C. Yim, D. Yoon, X. Zhang, X. Zhuang, L. Colombo, A. C. Ferrari and M. Garcia-Hernandez, *2D Mater.*, 2020, **7**, 022001.
- 25 M. D. Stoller, S. Park, Z. Yanwu, J. An and R. S. Ruoff, *Nano Lett.*, 2008, **8**, 3498–3502.
- 26 B. Kelly, *Physics of Graphite*: Applied Science Publishers, London Englewood NJ, 1981.
- 27 S. V. Morozov, K. S. Novoselov, M. I. Katsnelson, F. Schedin, D. C. Elias, J. A. Jaszczak and A. K. Geim, *Phys. Rev. Lett.*, 2008, **100**, 016602.
- 28 A. Boscá, J. Pedrós, J. Martínez and F. Calle, *J. Appl. Phys.*, 2015, **117**(4), 044504.
- 29 K. S. Novoselov, A. K. Geim, S. V. Morozov, D. Jiang, Y. Zhang, S. V. Dubonos, I. V. Grigorieva and A. A. Firsov, *Science*, 2004, **306**, 666–669.
- 30 C. Si, Z. Sun and F. Liu, *Nanoscale*, 2016, **8**, 3207–3217.



31 M. F. El-Kady, Y. Shao and R. B. Kaner, *Nat. Rev. Mater.*, 2016, **1**, 16033.

32 X. Cao, Z. Yin and H. Zhang, *Energy Environ. Sci.*, 2014, **7**, 1850–1865.

33 V. Chabot, D. Higgins, A. Yu, X. Xiao, Z. Chen and J. Zhang, *Energy Environ. Sci.*, 2014, **7**, 1564–1596.

34 Y. Wu, J. Zhu and L. Huang, *Carbon*, 2019, **143**, 610–640.

35 L. Dong, C. Xu, Y. Li, Z. H. Huang, F. Kang, Q. H. Yang and X. Zhao, *J. Mater. Chem. A*, 2016, **4**, 4659–4685.

36 Y. Zhu, S. Murali, M. D. Stoller, K. J. Ganesh, W. Cai, P. J. Ferreira, A. Pirkle, R. M. Wallace, K. A. Cychosz, M. Thommes, D. Su, E. A. Stach and R. S. Ruoff, *Science*, 2011, **332**, 1537–1541.

37 B. G. Choi, M. Yang, W. H. Hong, J. W. Choi and Y. S. Huh, *ACS Nano*, 2012, **6**, 4020–4028.

38 Z. Niu, J. Chen, H. H. Hng, J. Ma and X. Chen, *Adv. Mater.*, 2012, **24**, 4144–4150.

39 H. C. Tao, S. C. Zhu, X. L. Yang, L. L. Zhang and S. B. Ni, *Electrochim. Acta*, 2016, **190**, 168–177.

40 X. Cao, Y. Shi, W. Shi, G. Lu, X. Huang, Q. Yan, Q. Zhang and H. Zhang, *Small*, 2011, **7**, 3163–3168.

41 P. Romero, P. A. Postigo, E. Baquedano, J. Martínez, A. Boscá and R. Guzman de Villoria, *Chem. Eng. J.*, 2016, **299**, 8–14.

42 A. Boscá, J. Pedrós, J. Martínez, T. Palacios and F. Calle, *Sci. Rep.*, 2016, **6**, 21676.

43 S. Fernández, A. Boscá, J. Pedrós, A. Inés, M. Fernández, I. Arnedo, J. P. González, M. de la Cruz, D. Sanz, A. Molinero, R. S. Fandan, M. ángela Pampillón, F. Calle, J. J. Gandía, J. Cárate and J. Martínez, *Micromachines*, 2019, **10**, 402.

44 Z. Fan, J. Yan, L. Zhi, Q. Zhang, T. Wei, J. Feng, M. Zhang, W. Qian and F. Wei, *Adv. Mater.*, 2010, **22**, 3723–3728.

45 D. Yu and L. Dai, *J. Phys. Chem. Lett.*, 2010, **1**, 467–470.

46 B. You, L. Wang, L. Yao and J. Yang, *Chem. Commun.*, 2013, **49**, 5016–5018.

47 J. Chang, M. Jin, F. Yao, T. H. Kim, V. T. Le, H. Yue, F. Gunes, B. Li, A. Ghosh, S. Xie and Y. H. Lee, *Adv. Funct. Mater.*, 2013, **23**, 5074–5083.

48 Q. Cheng, J. Tang, J. Ma, H. Zhang, N. Shinya and L. C. Qin, *Carbon*, 2011, **49**, 2917–2925.

49 H. Wang, H. Yi, X. Chen and X. Wang, *J. Mater. Chem. A*, 2014, **2**, 3223–3230.

50 J. Yan, Z. Fan, W. Sun, G. Ning, T. Wei, Q. Zhang, R. Zhang, L. Zhi and F. Wei, *Adv. Funct. Mater.*, 2012, **22**, 2632–2641.

51 D. S. Patil, S. A. Pawar, J. C. Shin and H. J. Kim, *J. Power Sources*, 2019, **435**, 226812.

52 S. Liu, Y. Yin, K. San Hui, K. N. Hui, S. C. Lee and S. Chan Jun, *Electrochim. Acta*, 2019, **297**, 479–487.

53 S. Ruiz-Gómez, A. Boscá, L. Pérez, J. Pedrós, J. Martínez, A. Páez and F. Calle, *Diamond Relat. Mater.*, 2015, **57**, 63–67.

54 K. Zhang, L. L. Zhang, X. S. Zhao and J. Wu, *Chem. Mater.*, 2010, **22**, 1392–1401.

55 Q. Wu, X. Yuxi, Z. Yao, A. Liu and G. Shi, *ACS Nano*, 2010, **4**, 1963–1970.

56 Y. Gao, *Nanoscale Res. Lett.*, 2017, **12**, 387.

57 J. Pedrós, A. Boscá, J. Martínez, S. Ruiz-Gómez, L. Pérez, V. Barranco and F. Calle, *J. Power Sources*, 2016, **317**, 35–42.

58 M. F. El-Kady, V. Strong, S. Dubin and R. B. Kaner, *Science*, 2012, **335**, 1326–1330.

59 M. F. El-Kady and R. B. Kaner, *Nat. Commun.*, 2013, **4**, 1475.

60 L. Li, J. Zhang, Z. Peng, Y. Li, C. Gao, Y. Ji, R. Ye, N. D. Kim, Q. Zhong, Y. Yang, H. Fei, G. Ruan and J. M. Tour, *Adv. Mater.*, 2016, **28**, 838–845.

61 Z. Wan, E. W. Streed, M. Lobino, S. Wang, R. T. Sang, I. S. Cole, D. V. Thiel and Q. Li, *Adv. Mater. Technol.*, 2018, **3**, 1700315.

62 X. Y. Fu, Z. Di Chen, D. D. Han, Y. L. Zhang, H. Xia and H.-B. Sun, *Photon. Res.*, 2020, **8**, 577–588.

63 J. Wang, F. Li, F. Zhu and O. G. Schmidt, *Small Methods*, 2019, **3**, 1800367.

64 Z. Chen, W. Ren, L. Gao, B. Liu, S. Pei and H. M. Cheng, *Nat. Mater.*, 2011, **10**, 424–428.

65 S. Min, C. Zhao, G. Chen and X. Qian, *Electrochim. Acta*, 2014, **115**, 155–164.

66 J. Yang, E. Zhang, X. Li, Y. Yu, J. Qu and Z. Z. Yu, *ACS Appl. Mater. Interfaces*, 2016, **8**, 2297–2305.

67 X. Li, Z. Wang, Y. Qiu, Q. Pan and P. Hu, *J. Alloys Compd.*, 2015, **620**, 31–37.

68 J. Lv, Z. Wang and H. Miura, *Solid State Commun.*, 2018, **269**, 45–49.

69 G. Ren, R. Zhang and Z. Fan, *Appl. Surf. Sci.*, 2018, **441**, 466–473.

70 N. Van Hoa, T. T. H. Quyen, N. H. Nghia, N. Van Hieu and J. J. Shim, *J. Alloys Compd.*, 2017, **702**, 693–699.

71 L. Jinlong, Z. Wang, L. Tongxiang, Y. Meng, K. Suzuki and H. Miura, *J. Electroanal. Chem.*, 2017, **799**, 595–601.

72 X. Dong, J. Wang, J. Wang, M. B. Chan-Park, X. Li, L. Wang, W. Huang and P. Chen, *Mater. Chem. Phys.*, 2012, **134**, 576–580.

73 Y. Zhao, J. Liu, Y. Hu, H. Cheng, C. Hu, C. Jiang, L. Jiang, A. Cao and L. Qu, *Adv. Mater.*, 2013, **25**, 591–595.

74 J. Ren, R. P. Ren and Y. K. Lv, *Chem. Eng. J.*, 2018, **349**, 111–118.

75 J. Zhu, L. Kong, X. Shen, Q. Chen, Z. Ji, J. Wang, K. Xu and G. Zhu, *Appl. Surf. Sci.*, 2018, **428**, 348–355.

76 Q. Li, M. Horn, Y. Wang, J. MacLeod, N. Motta and J. Liu, *Materials*, 2019, **12**, 703.

77 X. Bai, Q. Liu, H. Zhang, J. Liu, Z. Li, X. Jing, Y. Yuan, L. Liu and J. Wang, *Electrochim. Acta*, 2016, **215**, 492–499.

78 T. Yin, W. Zhang, Y. Yin, Y. Yan, K. Zhan, J. Yang and B. Zhao, *J. Mater. Sci.: Mater. Electron.*, 2017, **28**, 7884–7891.

79 M. Yu, J. Chen, J. Liu, S. Li, Y. Ma, J. Zhang and J. An, *Electrochim. Acta*, 2015, **151**, 99–108.

80 S. Sun, S. Wang, S. Li, Y. Li, Y. Zhang, J. Chen, Z. Zhang, S. Fang and P. Wang, *J. Mater. Chem. A*, 2016, **4**, 18646–18653.

81 C. Zhang, T. Kuila, N. H. Kim, S. H. Lee and J. H. Lee, *Carbon*, 2015, **89**, 328–339.

82 J. Lv, T. Liang, M. Yang, S. Ken and M. Hideo, *J. Energy Chem.*, 2017, **26**, 330–335.

83 X. Feng, J. Ning, D. Wang, J. Zhang, M. Xia, Y. Wang and Y. Hao, *J. Alloys Compd.*, 2020, **816**, 152625.



84 H. Chen, C. K. Hsieh, Y. Yang, X. Y. Liu, C. H. Lin, C. H. Tsai, Z. Q. Wen, F. Dong and Y. X. Zhang, *ChemElectroChem*, 2017, **4**, 2414–2422.

85 L. H. Tseng, C. H. Hsiao, D. D. Nguyen, P. Y. Hsieh, C. Y. Lee and N. H. Tai, *Electrochim. Acta*, 2018, **266**, 284–292.

86 Z. Zhang, K. Chi, F. Xiao and S. Wang, *J. Mater. Chem. A*, 2015, **3**, 12828–12835.

87 X. Bai, Q. Liu, J. Liu, Z. Gao, H. Zhang, R. Chen, Z. Li, R. Li, P. Liu and J. Wang, *Chem. Eng. J.*, 2017, **328**, 873–883.

88 K. Chi, Z. Zhang, Q. Lv, C. Xie, J. Xiao, F. Xiao and S. Wang, *ACS Appl. Mater. Interfaces*, 2017, **9**, 6044–6053.

89 A. A. Mirghni, M. J. Madito, K. O. Oyedotun, T. M. Masikhwa, N. M. Ndiaye, S. J. Ray and N. Manyala, *RSC Adv.*, 2018, **8**, 11608–11621.

90 G. Saeed, S. Kumar, N. H. Kim and J. H. Lee, *Chem. Eng. J.*, 2018, **352**, 268–276.

91 L. G. Beka, X. Li and W. Liu, *Sci. Rep.*, 2017, **7**, 2105.

92 M. Yu, X. Li, Y. Ma, R. Liu, J. Liu and S. Li, *Appl. Surf. Sci.*, 2017, **396**, 1816–1824.

93 P. Miao, J. He, Z. Sang, F. Zhang, J. Guo, D. Su, X. Yan, X. Li and H. Ji, *J. Alloys Compd.*, 2018, **732**, 613–623.

94 S. J. Patil, J. H. Kim and D. W. Lee, *J. Power Sources*, 2017, **342**, 652–665.

95 P. Geng, S. Zheng, H. Tang, R. Zhu, L. Zhang, S. Cao, H. Xue and H. Pang, *Adv. Energy Mater.*, 2018, **8**, 1703259.

96 E. Kamali-Heidari, Z. L. Xu, M. H. Sohi, A. Ataie and J. K. Kim, *Electrochim. Acta*, 2018, **271**, 507–518.

97 Z. Kang, Y. Li, Y. Yu, Q. Liao, Z. Zhang, H. Guo, S. Zhang, J. Wu, H. Si, X. Zhang and Y. Zhang, *J. Mater. Sci.*, 2018, **53**, 10292–10301.

98 X. Cai, X. Shen, L. Ma, Z. Ji and L. Kong, *RSC Adv.*, 2015, **5**, 58777–58783.

99 A. M. Zardkhoshou and S. S. H. Davarani, *J. Colloid Interface Sci.*, 2019, **535**, 195–204.

100 R. Li, W. Zhang, M. Zhang, Z. Peng, Y. Wang, Y. Liu, Y. Zheng, X. Guo, Y. Zhang, Z. Wang and T. Zhang, *Mater. Chem. Phys.*, 2021, **257**, 123769.

101 S. Drieschner, M. Weber, J. Wohlkettetter, J. Vieten, E. Makrygiannis, B. M. Blaschke, V. Morandi, L. Colombo, F. Bonaccorso and J. A. Garrido, *2D Mater.*, 2016, **3**, 045013.

102 Z. Wang, H. Y. Yue, Z. M. Yu, S. Huang, X. Gao, B. Wang, S. S. Song, E. H. Guan, W. Q. Wang and H. J. Zhang, *Microchem. J.*, 2019, **147**, 163–169.

103 M. J. Madito, K. S. Matshoba, F. U. Ochai-Ejeh, N. Mongwaketsi, C. B. Mtshali, M. Fabiane and N. Manyala, *Surf. Coat. Technol.*, 2020, **383**, 125230.

104 W. Li, M. C. Tekell, C. Liu, J. A. Hethcock and D. Fan, *Adv. Funct. Mater.*, 2018, **28**, 1800601.

105 X. Xu, C. Guan, L. Xu, Y. H. Tan, D. Zhang, Y. Wang, H. Zhang, D. J. Blackwood, J. Wang, M. Li and J. Ding, *ACS Nano*, 2020, **14**, 937–947.

106 H. Park, J. W. Kim, S. Y. Hong, G. Lee, D. S. Kim, J. hyun Oh, S. W. Jin, Y. R. Jeong, S. Y. Oh, J. Y. Yun and J. S. Ha, *Adv. Funct. Mater.*, 2018, **28**, 1707013.

107 C. Liu, H. Liang, D. Wu, X. Lu and Q. Wang, *Adv. Electron. Mater.*, 2018, **4**, 1870034.

108 G. Li, Z. Meng, J. Qian, C. L. Ho, S. P. Lau, W. Y. Wong and F. Yan, *Mater. Today Energy*, 2019, **12**, 155–160.

109 K. Y. Kim, H. Choi, C. Van Tran and J. Bin, *J. Power Sources*, 2019, **441**, 227199.

110 C. Zhu, D. Zhao, K. Wang, X. Dong, W. Duan, F. Wang, M. Gao and G. Zhang, *J. Mater. Sci.*, 2019, **54**, 4192–4201.

111 J. Lin, Z. Peng, Y. Liu, F. Ruiz-Zepeda, R. Ye, E. L. G. Samuel, M. J. Yacaman, B. I. Yakobson and J. M. Tour, *Nat. Commun.*, 2014, **5**, 5714.

112 J. Bin In, B. Hsia, J. H. Yoo, S. Hyun, C. Carraro, R. Maboudian and C. P. Grigoropoulos, *Carbon*, 2015, **83**, 144–151.

113 A. Lamberti, F. Clerici, M. Fontana and L. Scaltrito, *Adv. Energy Mater.*, 2016, **6**, 1600050.

114 R. Arul, R. N. Oosterbeek, J. Robertson, G. Xu, J. Jin and M. C. Simpson, *Carbon*, 2016, **99**, 423–431.

115 Z. Wan, S. Wang, B. Haylock, J. Kaur, P. Tanner, D. Thiel, R. Sang, I. S. Cole, X. Li, M. Lobino and Q. Li, *Carbon*, 2019, **141**, 83–91.

116 G. Li, *J. Appl. Phys.*, 2020, **127**, 010901.

117 R. Ye, Y. Chyan, J. Zhang, Y. Li, X. Han, C. Kittrell and J. M. Tour, *Adv. Mater.*, 2017, **29**, 1702211.

118 Z. Zhang, M. Song, J. Hao, K. Wu, C. Li and C. Hu, *Carbon*, 2018, **127**, 287–296.

119 W. Zhang, Y. Lei, F. Ming, Q. Jiang, P. M. F. J. Costa and H. N. Alshareef, *Adv. Energy Mater.*, 2018, **8**, 1801840.

120 W. Zhang, Y. Lei, Q. Jiang, F. Ming, P. M. F. J. Costa and H. N. Alshareef, *Small Methods*, 2019, **3**, 1900005.

121 D. Bhattacharjya, C. H. Kim, J. H. Kim, I. K. You, J. Bin In and S. M. Lee, *Appl. Surf. Sci.*, 2018, **462**, 353–361.

122 T. X. Tran, H. Choi, C. H. Che, J. H. Sul, I. G. Kim, S. M. Lee, J. H. Kim and J. Bin In, *ACS Appl. Mater. Interfaces*, 2018, **10**, 39777–39784.

123 M. Parmeggiani, P. Zaccagnini, S. Stassi, M. Fontana, S. Bianco, C. Nicosia, C. F. Pirri and A. Lamberti, *ACS Appl. Mater. Interfaces*, 2019, **11**, 33221–33230.

124 F. Mahmood, F. Mahmood, H. Zhang, J. Lin and C. Wan, *ACS Omega*, 2020, **5**, 14611–14618.

125 R. Kumar, R. Savu, E. Joanni, A. R. Vaz, M. A. Canesqui, R. K. Singh, R. A. Timm, L. T. Kubota and S. A. Moshkalev, *RSC Adv.*, 2016, **6**, 84769–84776.

126 R. Kumar, E. Joanni, R. K. Singh, E. T. S. G. da Silva, R. Savu, L. T. Kubota and S. A. Moshkalev, *J. Colloid Interface Sci.*, 2017, **507**, 271–278.

127 S. M. B. Malek Hosseini, S. M. Baizaee, H. R. Naderi and A. Dare Kordi, *Appl. Surf. Sci.*, 2018, **427**, 507–516.

128 B. Xie, Y. Wang, W. Lai, W. Lin, Z. Lin, Z. Zhang, P. Zou, Y. Xu, S. Zhou, C. Yang, F. Kang and C. P. Wong, *Nano Energy*, 2016, **26**, 276–285.

129 R. Kumar, E. Joanni, R. Savu, M. S. Pereira, R. K. Singh, C. J. L. Constantino, L. T. Kubota, A. Matsuda and S. A. Moshkalev, *Energy*, 2019, **179**, 676–684.

130 X. Mao, W. Yang, X. He, Y. Chen, Y. Zhao, Y. Zhou, Y. Yang and J. Xu, *Mater. Sci. Eng., B*, 2017, **216**, 16–22.

131 G. Li, X. Mo, W. C. Law and K. C. Chan, *J. Mater. Chem. A*, 2019, **7**, 4055–4062.



132 F. Wang, X. Dong, K. Wang, W. Duan, M. Gao, Z. Zhai, C. Zhu and W. Wang, *Carbon*, 2019, **150**, 396–407.

133 K. Gholami Laelabadi, R. Moradian and I. Manouchehri, *ACS Appl. Energy Mater.*, 2020, **3**, 5301–5312.

134 F. Xiang, J. Zhong, N. Gu, R. Mukherjee, I. K. Oh, N. Koratkar and Z. Yang, *Carbon*, 2014, **75**, 201–208.

135 A. Borenstein, V. Strauss, M. D. Kowal, M. Yoonessi, M. Muni, M. Anderson and R. B. Kaner, *J. Mater. Chem. A*, 2018, **6**, 20463–20472.

136 E. Ghoniem, S. Mori and A. Abdel-Moniem, *J. Power Sources*, 2016, **324**, 272–281.

137 W. Song, J. Zhu, B. Gan, S. Zhao, H. Wang, C. Li and J. Wang, *Small*, 2018, **14**, 1702249.

138 E. C. Cho, C. W. Chang-Jian, W. L. Syu, H. S. Tseng, K. C. Lee, J. H. Huang and Y. S. Hsiao, *Appl. Surf. Sci.*, 2020, **518**, 146193.

139 A. Ladrón-de-Guevara, A. Boscá, J. Pedrós, E. Climent-Pascual, A. de Andrés, F. Calle and J. Martínez, *Appl. Surf. Sci.*, 2019, **467–468**, 691–697.

140 L. F. Zhang, J. Tang, S. Y. Liu, O. W. Peng, R. Shi, B. N. Chandrashekhar, Y. Li, X. Li, X. N. Li, B. M. Xu and C. Cheng, *Mater. Today Energy*, 2017, **5**, 222–229.

141 S. Yang, Y. Li, J. Sun and B. Cao, *J. Power Sources*, 2019, **431**, 220–225.

142 S. Yang, Y. Liu, Y. Hao, X. Yang, W. A. Goddard, X. L. Zhang and B. Cao, *Adv. Sci.*, 2018, **5**, 1700659.

143 F. Clerici, M. Fontana, S. Bianco, M. Serrapede, F. Perrucci, S. Ferrero, E. Tresso and A. Lamberti, *ACS Appl. Mater. Interfaces*, 2016, **8**, 10459–10465.

144 Z. Peng, R. Ye, J. A. Mann, D. Zakhidov, Y. Li, P. R. Smalley, J. Lin and J. M. Tour, *ACS Nano*, 2015, **9**, 5868–5875.

145 C. Zhou, M. Hong, Y. Yang, C. Yang, N. Hu, L. Zhang, Z. Yang and Y. Zhang, *J. Power Sources*, 2019, **438**, 227044.

146 S. M. Lee, Y. J. Park and J. H. Kim, *ACS Appl. Nano Mater.*, 2019, **2**, 3711–3717.

147 H. Liu, M. Li, R. B. Kaner, S. Chen and Q. Pei, *ACS Appl. Mater. Interfaces*, 2018, **10**, 15609–15615.

148 L. V. Thekkakara and M. Gu, *Sci. Rep.*, 2019, **9**, 11822.

149 N. Kamboj, T. Purkait, M. Das, S. Sarkar, K. S. Hazra and R. S. Dey, *Energy Environ. Sci.*, 2019, **12**, 2507–2517.

150 W. Wang, L. Lu, Y. Xie, W. Yuan, Z. Wan, Y. Tang and K. S. Teh, *Adv. Mater. Technol.*, 2020, **5**, 1900903.

151 A. D. Smith, Q. Li, A. Vyas, M. M. Haque, K. Wang, A. Velasco, X. Zhang, S. Thurakkal, A. Quellmalz, F. Niklaus, K. Gylfason, P. Lundgren and P. Enoksson, *Sensor*, 2019, **19**, 4231.

152 Y. Shao, J. Li, Y. Li, H. Wang, Q. Zhang and R. B. Kaner, *Mater. Horiz.*, 2017, **4**, 1145–1150.

153 Y. Yue, N. Liu, Y. Ma, S. Wang, W. Liu, C. Luo, H. Zhang, F. Cheng, J. Rao, X. Hu, J. Su and Y. Gao, *ACS Nano*, 2018, **12**, 4224–4232.

154 J. Yoo, S. Byun, C. W. Lee, C. Y. Yoo and J. Yu, *Chem. Mater.*, 2018, **30**, 3979–3990.

155 J. Ye, H. Tan, S. Wu, K. Ni, F. Pan, J. Liu, Z. Tao, Y. Qu, H. Ji, P. Simon and Y. Zhu, *Adv. Mater.*, 2018, **30**, 1801384.

156 T. Purkait, G. Singh, N. Kamboj, M. Das and R. S. Dey, *J. Mater. Chem. A*, 2018, **6**, 22858–22869.

157 J. Gao, C. Shao, S. Shao, C. Bai, U. R. Khalil, Y. Zhao, L. Jiang and L. Qu, *ACS Nano*, 2019, **13**, 7463–7470.

158 T. Wang, L. Li, X. Tian, H. Jin, K. Tang, S. Hou, H. Zhou and X. Yu, *Electrochim. Acta*, 2019, **319**, 245–252.

159 F. Zhou, H. Huang, C. Xiao, S. Zheng, X. Shi, J. Qin, Q. Fu, X. Bao, X. Feng, K. Müllen and Z. S. Wu, *J. Am. Chem. Soc.*, 2018, **140**, 8198–8205.

160 C. Couly, M. Alhabeb, K. L. Van Aken, N. Kurra, L. Gomes, A. M. Navarro-Suárez, B. Anasori, H. N. Alshareef and Y. Gogotsi, *Adv. Electron. Mater.*, 2018, **4**, 1700339.

161 H. Xiao, Z. S. Wu, F. Zhou, S. Zheng, D. Sui, Y. Chen and X. Bao, *Energy Storage Mater.*, 2018, **13**, 233–240.

162 J. Qin, J. Gao, X. Shi, J. Chang, Y. Dong, S. Zheng, X. Wang, L. Feng and Z. S. Wu, *Adv. Funct. Mater.*, 2020, **30**, 1909756.

163 X. Shi, S. Pei, F. Zhou, W. Ren, H. M. Cheng, Z. S. Wu and X. Bao, *Energy Environ. Sci.*, 2019, **12**, 1534–1541.

164 J. K. Chih, A. Jamaluddin, F. Chen, J. K. Chang and C. Y. Su, *J. Mater. Chem. A*, 2019, **7**, 12779–12789.

165 Y. Liu, B. Zhang, Q. Xu, Y. Hou, S. Seyedin, S. Qin, G. G. Wallace, S. Beirne, J. M. Razal and J. Chen, *Adv. Funct. Mater.*, 2018, **28**, 1706592.

166 R. Agrawal and C. Wang, *Micromachines*, 2018, **9**, 399.

167 L. Naderi, S. Shahrokhian and F. Soavi, *J. Mater. Chem. A*, 2020, **8**, 19588–19602.

168 C. Zhu, X. Dong, X. Mei, M. Gao, K. Wang and D. Zhao, *J. Mater. Sci.*, 2020, **55**, 17108–17119.

169 A. Tiliakos, A. M. I. Trefilov, E. Tanasă, A. Balan and I. Stamatin, *J. Power Sources*, 2018, **384**, 145–155.

170 H. Wu, W. Zhang, S. Kandambeth, O. Shekhah, M. Eddaoudi and H. N. Alshareef, *Adv. Energy Mater.*, 2019, **9**, 1900482.

171 G. Bhattacharya, S. J. Fishlock, A. Pritam, S. Sinha Roy and J. A. McLaughlin, *Adv. Sustainable Syst.*, 2020, **4**, 1900133.

172 X. Yu, N. Li, S. Zhang, C. Liu, L. Chen, S. Han, Y. Song, M. Han and Z. Wang, *J. Power Sources*, 2020, **478**, 229075.

173 H. Liu, K. sik Moon, J. Li, Y. Xie, J. Liu, Z. Sun, L. Lu, Y. Tang and C. P. Wong, *Nano Energy*, 2020, **77**, 105058.

174 R. Xu, P. Liu, G. Ji, L. Gao and J. Zhao, *ACS Appl. Energy Mater.*, 2020, **3**, 10676–10684.

175 D. Shen, G. Zou, L. Liu, W. Zhao, A. Wu, W. W. Duley and Y. N. Zhou, *ACS Appl. Mater. Interfaces*, 2018, **10**, 5404–5412.

176 H. Pan, D. Wang, Q. Peng, J. Ma, X. Meng, Y. Zhang, Y. Ma, S. Zhu and D. Zhang, *ACS Appl. Mater. Interfaces*, 2018, **10**, 10157–10164.

177 M. Z. Esfahani and M. Khosravi, *J. Power Sources*, 2020, **462**, 228166.

178 C. Kim, D. Y. Kang and J. H. Moon, *Nano Energy*, 2018, **53**, 182–188.

179 J. Li, M. Zhu, Z. An, Z. Wang, M. Toda and T. Ono, *J. Power Sources*, 2018, **401**, 204–212.

180 J. Lin, C. Zhang, Z. Yan, Y. Zhu, Z. Peng, R. H. Hauge, D. Natelson and J. M. Tour, *Nano Lett.*, 2013, **13**, 72–78.

181 C. Shen, S. Xu, Y. Xie, M. Sanghadasa, X. Wang and L. Lin, *J. Microelectromech. Syst.*, 2017, **26**, 949–965.

182 S. Oukassi, R. Salot, A. Bazin, C. Secouard, I. Chevalier, S. Poncelet, S. Poulet, J. M. Boissel, F. Geffraye and J. Brun, *Tech. Dig. - Int. Electron Devices Meet. IEDM*, 2019, **2019**, 618–621.

